

Unconventional band structure via combined molecular orbital and lattice symmetries in a surface-confined metallated graphdiyne sheet

Ignacio Piquero-Zulaica^{1,†,*}, Wenqi Hu^{2,†}, Ari Paavo Seitsonen^{3,†}, Felix Haag¹, Johannes K  chle¹, Francesco Allegretti¹, Yuanhao Lyu², Lan Chen², Kehui Wu², Zakaria M. Abd El-Fattah⁴, Ethem Akt  rk⁵, Svetlana Klyatskaya⁶, Mario Ruben^{6,7}, Matthias Muntwiler⁸, Johannes V. Barth^{1,*} and Yi-Qi Zhang^{2,1*}

¹*Physics Department E20, Technical University of Munich, D-85748 Garching, Germany*

²*Institute of Physics, Chinese Academy of Sciences, 100190 Beijing, China*

³*D  partement de Chimie,   cole Normale Sup  rieure, 24 rue Lhomond, F-75005 Paris, France*

⁴*Physics Department, Faculty of Science, Al-Azhar University, Nasr City, E-11884, Cairo, Egypt*

⁵*Department of Physics, Adnan Menderes University, 09100 Aydin, Turkey*

⁶*Institute of Nanotechnology, Karlsruhe Institute of Technology, 76344 Eggenstein-Leopoldshafen, Germany*

⁷*IPCMS-CNRS, Universit   de Strasbourg, 23 rue de Loess, 67034 Strasbourg, France*

⁸*Paul Scherrer Institute, Forschungsstrasse 111, 5232 Villigen PSI, Switzerland*

†These authors contributed equally.

*Email: ge46biq@mytum.de; jvb@tum.de; yiqi.zhang@iphy.ac.cn

Abstract

Graphyne (GY) and graphdiyne (GDY)-based materials represent an intriguing class of two-dimensional (2D) carbon-rich networks with tunable structures and properties surpassing those of graphene. However, the challenge of fabricating atomically well-defined crystalline GY/GDY-based systems largely hinders detailed electronic structure characterizations. Here, we report the emergence of an unconventional band structure in mesoscopically regular ($\sim 1 \mu\text{m}$) metallated GDY sheets featuring a honeycomb lattice on Ag(111) substrates. Employing complementary scanning tunnelling and angle-resolved photoemission spectroscopies, electronic band formation with a gap of 2.5 eV is rigorously determined in agreement with real-space electronic characteristics. Extensive density functional theory calculations corroborate our observations as well as recent theoretical predictions that doubly degenerate frontier molecular orbitals on a honeycomb lattice give rise to flat, Dirac and Kagome bands close to Fermi level. These results illustrate the tremendous potential of engineering novel band structures via molecular orbital and lattice symmetries in atomically precise 2D carbon scaffolds.

Synthesizing and characterizing π -conjugated two-dimensional (2D) polymers with atomic thickness and covalently bonded periodic structures has recently been pushed to the forefront of research in chemistry and physics¹⁻⁴, concomitant with the rapidly advancing exploration of 2D materials⁵⁻⁷. Through a suitable choice of molecular building blocks and linking motifs, crystalline 2D organic polymers or hybrid metal-organic sheets can be rationally designed to display principal electronic properties like π -orbital overlapping, dispersive bands as well as adjustable band gap^{8,9}, which are essential for organic electronics applications^{10,11}. In particular, theoretical modelling shows that a proper combination of frontier molecular orbital (MO) and lattice symmetries provides a new avenue towards realizing unconventional band structures in these materials, such as flat, Dirac and Kagome bands¹²⁻¹⁵, which can be further tailored to give rise to novel topological or many-body states^{13,14,16}.

Among various types of π -conjugated 2D polymers, a special class of carbon-based networks distinct from graphene, known as graphyne (GY)¹⁷ and graphdiyne (GDY)¹⁸ is of particular interest^{3,19}. Acetylenic precursors containing carbon-carbon triple bonds ($-\text{C}\equiv\text{C}-$) enable a combination of sp - and sp^2 -hybridized carbon atoms to create a great variety of GY/GDY-related structures²⁰, presenting remarkable tunability in their physical and chemical properties^{19,21}. However, synthesizing crystalline GY/GDY sheets as well as their analogues turned out to be particularly challenging¹⁹, which hampers in-depth electronic structure characterizations. The past fifteen years witnessed the rapid growth in the field of on-surface synthesis in ultra-high vacuum (UHV)^{22,23}, giving new access to synthesize 2D polymers via the bottom-up approach²⁴, and many exemplary carbon-based architectures have been achieved²⁵⁻²⁹. Utilizing a terminal alkyne derivative 1,3,5-tris(4-ethynylphenyl)benzene (Ext-TEB)³⁰ and a highly chemoselective gas-mediated on-surface reaction protocol, we recently fabricated a highly regular mesoscale ($\sim 1 \mu\text{m}$) organometallic monolayer³¹, formally representing an Ag-metallated graphdiyne (Ag-GDY) analogue. Therefore, it provides an ideal

platform to scrutinize the electronic properties of atomically well-defined metallated GDY sheets.

In this work, employing scanning tunnelling microscopy and spectroscopy (STM/STS), angle-resolved photoelectron spectroscopy (ARPES) and density functional theory (DFT), we demonstrate that the intrinsic electronic structure of Ag-GDY corresponds to a hole-doped semiconductor with an unconventional band structure. Notably, both the conduction band minimum and the valence band maximum comprise nontrivial flat bands, resulting from the combined molecular orbital and lattice symmetries. The band formation together with a gap of ≈ 2.5 eV is rigorously determined via STS and ARPES characterization, whereby a charge transfer from the substrate to the network is induced by mild electronic hybridization. DFT calculations corroborate the experimental results and further reveal that employing an insulating buffer layer may restore the Ag-GDY intrinsic band structure with a flat band lying near the Fermi level, which is important for tuning correlated electronic behaviour in such systems.

Results

Emerging novel band structure in freestanding Ag-GDY. The Ag-GDY network (cf. chemical scheme in right panel of Fig. 1b) presents unique structural characteristics, featuring a honeycomb lattice occupied by Ext-TEB molecules and a Kagome lattice spanned by alkynyl-Ag atoms (cf. highlighted grids in Fig. 1b, left panel). Therefore, the Ag-GDY network is expected to harbour dispersive bands as Ext-TEB is aromatic³² and the Ag-intercalated butadiyne bridge ($-\text{C}\equiv\text{C}-\text{Ag}-\text{C}\equiv\text{C}-$) has covalent character³³. As a first step, the electronic band structure of the freestanding layer with a rhombic unit cell containing two Ext-TEB molecules and three silver atoms was calculated (cf. Fig. 1c and Supplementary Fig. 1). The conduction bands (CBs) of the network start at ~ 2.4 eV above the Fermi level (Fig. 1c). The first group (CB₁) features two Dirac bands sandwiched between two nearly flat bands, whereas

the second group (CB₂) contains only two Dirac bands. The valence bands (VBs) reach 0.03 eV above the Fermi level, comprising two consecutive sets of Kagome bands (cf. VB₁ and VB₂ in Fig. 1c). It is unusual that lowest CB and highest VB are both flat bands, and these features are reminiscent of the typical band structure predicted from a honeycomb lattice with doubly degenerate on-site orbitals¹²⁻¹⁴.

To further examine the network band structure characteristics, MOs of Ext-TEB were calculated (cf. Fig. 1a and Supplementary Fig. 2). Both lowest unoccupied and highest occupied MOs (LUMO/HOMO) display double degeneracy, related to the three-fold symmetry of the molecule (Fig. 1a). DFT calculations also show that LUMO+1 and HOMO-1 for Ext-TEB are single levels with different energy separation ΔE to LUMO and HOMO (Fig. 1a), respectively.

The band structure of the Ag-GDY network can be interpreted based on a tight-binding model, as outlined by Ni et al¹³, employing a three-orbital (σ , π_x , π_y) basis on a honeycomb lattice, which results in six bands. If the energy separation ΔE between the degenerate (π_x , π_y)-MOs and the single σ -MO is large ($\Delta E = 0.4$ eV; red box in Fig. 1a), the former yields four bands with exact characteristics of CB₁ (Fig. 1c) and the latter produces two Dirac bands (CB₂). Alternatively, a small ΔE ($\Delta E = 0.23$ eV; blue box in Fig. 1a) will cause hybridization between σ and (π_x , π_y)-MOs, yielding two sets of Kagome bands¹³, representing the Ag-GDY valence band edge (VB₁ and VB₂ in Fig. 1c). To further verify the band composition, isosurfaces of orbital density integrated within the selected band groups were plotted (Fig. 1d). The orbital characters of CB₁ and CB₂ clearly correspond to LUMO and LUMO+1, respectively, and a similar correlation with HOMO and HOMO-1 exists for the VBs (cf. also Supplementary Fig. 2). Therefore, the emergence of flat, Dirac as well as Kagome bands close to the Fermi level can be rationalized based on the frontier MO and lattice symmetries of the Ag-GDY network. Another intriguing feature of the band structure is that the Fermi level intersects slightly below

the flat top VB, which is attributed to the open shell character of the alkynyl-Ag bridge³³⁻³⁵. Accordingly, isolated Ag-GDY sheets show hole-doped semiconductor characteristics with leading flat bands enclosing a gap of $E_g \approx 2.4$ eV.

Extended LDOS characteristics in a single Ag-GDY layer. High-quality samples are essential for electronic property characterization. The overview STM image in Figure 2a depicts the regular Ag-GDY network prepared on the Ag(111) single crystal surface, covering continuously an area of $\sim 500 \times 500$ nm² without apparent defects (cf. also Supplementary Fig. 3). The long-range order of the atomically thin film is also evidenced by the corresponding exemplary low-energy electron diffraction (LEED) pattern displayed in Fig. 2b. The LEED spots can be modelled via the superposition of three equivalent rectangular lattices along high-symmetry directions of Ag(111)³¹ (cf. Fig. 2c and Supplementary Fig. 4). For practical purposes, we also prepared Ag-GDY networks on inexpensive Ag(111)/mica. Notably, the atomically straight steps along high-symmetry directions favour continuous network growth across adjacent terraces (see Fig. 2d and Supplementary Fig. 5). This single layer continuity resembles the main feature of covalently bonded 2D materials (e.g., *h*-BN or graphene sheets)^{36,37}. On both substrates the network unit cell is rectangular, with parameters $a_1 = 63.6$ Å, $a_2 = 35.0$ Å (cf. Fig. 2f and Supplementary Fig. 7).

To unravel band formation in Ag-GDY, site-dependent differential conductance (dI/dV or STS) spectra as well as bias-dependent dI/dV maps were obtained, focusing on a six-membered ring as basic constituent of the regular network (cf. Fig. 3c). Hereby care must be taken to differentiate the appearance of the well-known quantum confinement effects imposed by the nanoporous lattice³⁸ on the quasi-2D electron gas provided by the Ag(111) surface state (SS) from the electronic properties of the Ag-GDY sheet.

Fig. 3a depicts point spectra recorded on Ag surface (black and grey curves), Ext-TEB molecules (red) and alkynyl-Ag atoms (blue) in a bias range from -0.2 to 1.2 V. The data taken

at the pore centre (black curve) displays three main peaks at 81, 328 and 677 mV, which correspond to the first, second and fourth ($n=1, 2, 4$) resonances of confined substrate Shockley-SS electrons in the nanocavity³⁸ (not related to the 2D polymer). The solid red curve in Fig. 3a is averaged over six molecular sites in the hexagonal unit (red mark in Fig. 3c). Genuine band formation is firstly evidenced by the fact that the dI/dV spectra taken at six molecular sites are nearly identical (cf. dimmed red curves in Fig. 3a), whereas this conformity was absent in isolated hexamers or disordered network patches (cf. Supplementary Fig. 8). The second indication is given by the emergence of a peak with onset at 464 mV, followed by three further peaks when sweeping up to 1000 mV (respectively indicated by a red arrow and black bars in Fig. 3a), which energy positions correspond neither to confined SS electrons nor to single Ext-TEB units, being featureless in this bias range³². The spectrum taken on the alkynyl-Ag atoms shows merely a steadily increasing intensity (Fig. 3a). Figure 3b displays dI/dV spectra taken at the same positions with a larger bias range. Again, their shapes do not vary at equivalent sites. The averaged spectrum on Ext-TEB units peaks at ~2200 mV, whereas for the Ag-bridge sites a single broad peak dominates at ~2050 mV, markedly downshifted when compared to the characteristic signature at 2.9 V of an individual Ag adatom on Ag(111)³⁹.

Real-space electronic states associated with SS confinement and intrinsic Ag-GDY band formation appear clearly in bias-dependent dI/dV maps (Fig. 3d) with energy positions indicated in Fig. 3a,b. At low biases, the imaged local density of states (LDOS) within the nanopore reflects typical intensity patterns of confined SS electrons ($n=1$ and 2; Fig. 3d-1,2). For a bias V_B of 464 mV (Figs. 3d-3), localized LDOS intensity clearly appears on the triangular-shaped Ext-TEB backbone, whence it is associated with the conduction band minimum (CBM; cf. Fig. 3a). With further increasing bias the LDOS extends to the Ag-bridge sites, until a uniform honeycomb grid evolves at 677 mV, indicating delocalized electronic character (Figs. 3d-4,5 and Supplementary Fig. 9). From 756 mV to 955 mV, the LDOS

concentrates at the alkynyl-Ag atoms (Fig. 3d-6,7). Most intriguing is the bias range from 1053 mV to 1355 mV, where the electron density at the molecular edge becomes prominent and merges via the alkynyl-Ag sites to form a marked Kagome grid at 1355 mV (Fig. 3d-8-10 and Supplementary Fig. 10). Examining the even higher bias range from 1.5 V to 2.2 V, the electronic Kagome grid becomes gradually filled until a nodal plane develops at the Ag-bridge (Fig. 3d-11-14).

The continuous evolution of LDOS pattern following the network topology manifests band characteristics in the Ag-GDY sheet. To search for the VBs (Fig. 1c), STS measurements also explored the bias range below the Fermi level, however, no significant features were observed (see Supplementary Fig. 11), similarly to other reported covalent structures adsorbed on metal substrates^{33,40}.

ARPES observation of valence-band formation. To probe the electronic properties of Ag-GDY in the occupied states regime, complementary ARPES measurements were carried out for networks grown on Ag(111) providing a sharp LEED pattern (cf. Fig. 2b and Supplementary Fig. 12). As reference the band structure $E(k_y)$ of a clean substrate measured along the $\overline{\Gamma K}$ direction of the Ag(111) surface Brillouin zone (BZ) with a photon energy of 62 eV is depicted in Fig. 4a. The well-known Ag SS surrounded by the projected bulk bands as well as the highly-dispersive *sp*-bands prevail. Since the silver *d*-bands' onset energy is 3.5 eV below the Fermi level (cf. Supplementary Fig. 13), a wide energy window for screening of Ag-GDY bands exists. Next, the occupied frontier orbitals of the intact Ext-TEB molecules were examined using an organic multilayer sample, whereby the nondispersive HOMO and HOMO-1 levels at $E_b \approx 2.8$ and 3.2 eV can be clearly discerned with maximal intensity at $\sim 1.5 \text{ \AA}^{-1}$, i.e., no delocalized states exist for the supramolecular assembly^{41,42} (Figs. 4b and Supplementary Fig. 14).

In Figure 4c, the band structure for the Ag-GDY fully covering the surface is shown. The previously distinct molecular orbitals of individual Ext-TEB (Fig. 4b) transform into less prominent intensity features smeared out along the $\overline{\Gamma K}$ direction in an energy window between $E_b \approx 2$ and 3 eV (cf. also Supplementary Fig. 15c). The VB formation is clearly recognized in Fig. 4d when comparing the energy distribution curves (EDCs) of pristine molecules and Ag-GDY extracted in the vicinity of $k_y=1.35 \text{ \AA}^{-1}$ in Fig. 4a-c. The HOMO (H) and HOMO-1 (H-1) peaks (grey curve in Fig. 4d) are well separated above the onset of the d -bands (purple area at $E_b > 3.8$ eV), in agreement with the DFT calculation (Fig. 1a). By contrast, for the adsorbed Ag-GDY sheet, a wider double-peak feature with an onset shifted closer to the Fermi level at $E_b \approx 2.0$ eV appears, followed by a much broader increase merged into the silver d -bands ($E_b \approx 3.8$ eV). The first set of VBs (denoted by VB'_1) has a relatively wide bandwidth of ~ 0.8 eV with clear intensity variations, indicating a fine structure due to multiple band contributions (cf. also Supplementary Fig. 15c). The higher intensity appearing at increased binding energies is attributed to the next set of bands denoted by VB'_2 . Obviously, the valence band maximum (VBM) of the adsorbed system shifts below the Fermi level compared to the freestanding layer (Fig. 1c), for reasons to be clarified below. Moreover, in Fig. 4e ARPES data for a photon energy of 100eV are reproduced such that the projection of the bulk bands around the $\overline{\Gamma}$ point is strongly attenuated, leading to a better recognition of the VBs. It is evident that VB'_1 and VB'_2 do not change their position with photon energy, whereas the intensity and the $E(k)$ distribution of the highly dispersive silver sp -bands are altered (cf. also Supplementary Fig. 16)⁴³, substantiating the conclusion that these VBs originate from the Ag-GDY sheet⁴⁴.

DFT modelling of adsorbed Ag-GDY network. To develop a better understanding of the experimental results, we carried out systematic DFT calculations of Ag-GDY sheet on a thick Ag(111) slab (cf. Methods). Fig. 5a displays the projected density of states (PDOS) of the system. In the unoccupied regime, the energy positions of CBM, the PDOS peak at 1 eV and

the double-peak feature at 2 eV agree well with the STS observations (cf. Figs. 3a,b and 5a). In the occupied regime, the VBM sets in at -1.2 eV, followed by two main peaks at -1.7 eV and -2.7 eV (Fig. 5a), which can be nicely correlated with the VB'_1 and VB'_2 in the ARPES data (cf. Fig. 4d). Note that the combined evidence from STS and ARPES data defines a gap size of 2.5 eV. It is well known that DFT calculations usually underestimate gap sizes, whence the obtained DFT value of $E_g \approx 1.7$ eV is rather satisfactory. Fig. 5b displays a series of simulated dI/dV maps. There is clearly a good match between experimental and simulated images in the appropriate energy ranges. Firstly, the confined Ag SS resonances ($n = 1,2$) in the nanopore are nicely reproduced due to the employed thick Ag slab (Fig. 5b-1,2; cf. also Supplementary Fig. 17). Secondly, typical bias-dependent LDOS patterns of the network are captured: starting from localized density on the Ext-TEB core (Fig. 5b-3) to displaying a uniform honeycomb electronic pathway (Fig. 5b-4), followed by merging of Ag-bridge (Fig. 5b-5) and molecular edge state (Fig. 5b-6) into a real-space electronic Kagome grid (Fig. 5b-7). Overall, the DFT calculations of the full system are in good agreement with the experimental observations.

Compared to the freestanding network, the VBs of the adsorbed layer on the silver surface notably shift below the Fermi level, indicating that the open shell of the unit cell is filled. An estimate obtained with the Bader charge analysis identified a total charge transfer of ≈ 3 electrons from the substrate as well as the bridging silver adatom to compensate six alkynyl radicals in the unit cell. Moreover, the absence of well-defined Kagome-type $E(k)$ relations in the ARPES data can be ascribed to a mild electronic hybridization between the adlayer and the silver surface (cf. Supplementary Fig. 18-20) as well as to a small BZ of the network. Nevertheless, at CBM ($V_B = 464$ mV) the LDOS intensity localized on the molecules captured in the experimental as well as simulated dI/dV maps (Figs. 3d-c and 5b-3) is compatible with the nontrivial-flat-band character, namely, quenched electron kinetic energy due to destructive interference of Bloch waves¹⁴.

Finally, in order to determine whether the intrinsic Ag-GDY electronic bands would be retained on an insulator, a sheet supported on a *h*-BN monolayer was modelled (Fig. 6a). Importantly, the leading VBs remain identical as those of the freestanding layer, and CB₁ and CB₂ slightly shift down toward the Fermi level (Fig. 6c). Notably, a finite (~ 37 meV) gap opens at the Γ point, which gives rise to an isolated flat band at the bottom of CB₁ (cf. red solid lines in Fig. 6c). Also, gap-opening at Dirac point can be observed for both CB₁ (~ 30 meV) and CB₂ (~ 37 meV). Note that the phenyl rings of individual Ext-TEB molecule in the unit cell locate on either nitrogen or boron atoms (Fig. 6a). Therefore, the adsorption-induced geometrical symmetry breaking provides another effective way to open band gaps^{14,16}.

Discussion

The realization of high-quality crystalline Ag-GDY sheets permitted an in-depth electronic structure characterization at both the atomic and mesoscopic scales. Band formation with a semiconducting gap of ≈ 2.5 eV was rigorously determined in this π -conjugated GDY analogue. Moreover, we reveal that Ag-GDY hosts unconventional flat, Dirac and Kagome bands at both conduction and valance band edges, which originate from combined MO and lattice symmetries. Although mild hybridization between the network and metal surface interferes, we show the possibility to restore the intrinsic band structure via electronic decoupling. Based on our results, replacing the molecular units and different metallation schemes can be envisioned. Therefore, the proper combination of MO characteristics and lattice symmetry can give access to bespoke novel electronic structures, unfolding exciting opportunities for tailored 2D material developments amenable to device-integrated applications.

Methods

Sample preparation. The Ag-GDY networks were prepared under ultrahigh vacuum conditions. Ag(111) single crystals and Ag(111)/mica substrates were used for sample growth. 1,3,5-tris(4-ethynylphenyl)benzene (Ext-TEB) precursors were evaporated from Al₂O₃ or quartz crucibles onto clean Ag(111) surfaces held at 200 K ~ 300 K, followed by an alkyne deprotonation procedure via introducing O₂ gas (≈ 6000 L) into the preparation chamber by backfilling via a leak valve. The sample was mildly annealed ($T_{\text{ann}} \approx 400$ K) to facilitate the organometallic network formation.

STM/STS characterization. A commercial Joule-Thomson STM (JT-STM, SPECS) and a homemade LT-STM were used for data acquisition. Data was recorded at an equilibrium temperature of ~ 5 K. Point STS spectroscopy were measured via a lock-in amplifier with a bias modulation of 20 mV at 676 Hz. dI/dV maps were recorded at fixed bias voltage in a grid with 128×128 pixels, and the feedback was switched off during dI/dV signal acquisition at each pixel. All the dI/dV maps were normalized via applying $(dI/dV)/(I/V)$, which leads a better signal to noise ratio without altering the LDOS features.

ARPES measurements. The ARPES experiments presented in this work were carried out at the Photo-Emission and Atomic Resolution Laboratory (PEARL) of the Swiss Light Source (SLS). The PEARL beamline delivers tunable soft X-ray photons in the energy range from 60 to 2000 eV with a resolving power up to $E/\Delta E = 7000$. In the present work we used photon energies of 62 eV and 100 eV to maximize the surface sensitivity. Samples are mounted on a high-precision manipulator with three translation and three rotation axes. Photoelectrons are detected by a Scienta EW4000 wide acceptance angle analyser with a two-dimensional multi-channel plate detector where one axis corresponds to the kinetic energy of the electron and the other axis to the emission angle. The entrance lens stack of the analyser is at a fixed angle of 60° with respect to the incoming synchrotron light. The X-ray beam, the polarization vector of photons, and the axis of the analyser lens are oriented horizontally, while the entrance slit of the electron analyser is oriented vertically. Samples were measured either at RT or at 60 K.

DFT calculations. Total energy calculations were performed using DFT within the Kohn–Sham formalism⁴⁵ using the Quantum ESPRESSO code⁴⁶. We used the rB86-vdW-DF2 approximation in the term of the exchange-correlation functional⁴⁷, and only the $\bar{\Gamma}$ point in the integration over the first Brillouin zone due to the very large super-cell. Projector augmented wave⁴⁸ data sets were applied to remove the core electron from the explicit calculation. STM simulations were performed with the Tersoff–Hamann model⁴⁹ approximating an s -wave tip.

We performed the calculations of the supported network in a hexagonal super-cell, unlike in Ref [31], where we used a rectangular, elongated cell. In order to reduce the stress in the overlayer we slightly adjusted the lateral lattice constant of the substrate to 4.18794 Å so that the average distance between the bridging Ag ad-atoms was the same as in the large system. During the relaxation and analysis of the electronic structure we used four layers of the substrate and a passivating layer of hydrogen at the bottom of the slab, and each layer of the substrate and the passivating layer consisted of 147 atoms, yielding a lateral lattice constant of 35.904 Å. In the calculations of the band structure, we could afford to include only two top-

most layers of substrate layers. The cut-off energies for wave functions and the electron density were 35 and 500 Ry, respectively.

In the calculation of the Ag-GDY network on the *h*-BN, 196 unit cells of latter were included with the same Ag-GDY network parameters as those for the silver substrate, whereby all the atoms were allowed to relax in any direction.

Acknowledgements

This work is financially supported by the National Natural Science Foundation of China (12174431 and 11825405) and the Strategic Priority Research Program of the Chinese Academy of Sciences (XDB30000000). J.V.B. acknowledges support from ERC (Advanced Grant MolArt), and the Munich Quantum Center, and the DFG Excellence Cluster e-conversion. F.H., J.K. and F.A. acknowledge funding by the German Research Foundation (DFG) through the TUM International Graduate School of Science and Engineering (IGSSE, GSC81). We gratefully acknowledge the Paul Scherrer Institut (Villigen, Switzerland) for the provision of synchrotron radiation beamtime at beamline PEARL of the Swiss Light Source (SLS). We also thank Willi Auwärter for helpful discussions.

Author contributions

Y.-Q.Z., I.P.-Z. and J.V.B. conceived the experiments. I.P.-Z. led the ARPES measurements and analysed the data with contribution from Y.-Q.Z., F.H., J.K. F.A. and M.M.. W.H., Y.L., Y.-Q.Z., L.C., and K.W. performed the STM/STS experiments and analysed the data. A.P.S. carried out the DFT calculations. Z.M.A.E.-F. carried out confined-surface-states analysis. E.A. performed tight-binding modelling. S.K. and M.R. developed the synthesis of the molecules used. Y.-Q.Z., I.P.-Z., A.P.S. and J.V.B. co-wrote the paper with contribution from all authors.

Competing interests

The authors declare no competing interests.

Additional information

Supplementary information is available for this paper.

References

1. Sakamoto, J., van Heijst, J., Lukin, O. & Schlüter, A. D. Two-dimensional polymers: just a dream of synthetic chemists? *Angew. Chem. Int. Edit.* **48**, 1030-1069 (2009).
2. Colson, J. W. & Dichtel, W. R. Rationally synthesized two-dimensional polymers. *Nat. Chem.* **5**, 453-465 (2013).
3. Hirsch, A. The era of carbon allotropes. *Nat. Mater.* **9**, 868-871 (2010).
4. Backes, C., *et al.* Production and processing of graphene and related materials. *2D Materials* **7**, 022001 (2020).
5. Mas-Ballesté, R., Gómez-Navarro, C., Gómez-Herrero, J. & Zamora, F. 2D materials: to graphene and beyond. *Nanoscale* **3**, 20-30 (2011).
6. Butler, S. Z., *et al.* Progress, challenges, and opportunities in two-dimensional materials beyond graphene. *ACS Nano* **7**, 2898-2926 (2013).
7. Novoselov, K. S., Mishchenko, A., Carvalho, A. & Neto, A. H. C. 2D materials and van der Waals heterostructures. *Science* **353**, aac9439 (2016).

8. Gutzler, R. Band-structure engineering in conjugated 2D polymers. *Phys. Chem. Chem. Phys.* **18**, 29092-29100 (2016).
9. Gutzler, R. & Perepichka, D. F. π -electron conjugation in two dimensions. *J. Am. Chem. Soc.* **135**, 16585-16594 (2013).
10. Fahlman, M., *et al.* Interfaces in organic electronics. *Nat. Rev. Mater.* **4**, 627-650 (2019).
11. Liu, Y., Duzhko, V. V., Page, Z. A., Emrick, T. & Russell, T. P. Conjugated polymer zwitterions: Efficient interlayer materials in organic electronics. *Acc. Chem. Res.* **49**, 2478-2488 (2016).
12. Wu, C., Bergman, D., Balents, L. & Das Sarma, S. Flat bands and Wigner crystallization in the honeycomb optical lattice. *Phys. Rev. Lett.* **99**, 070401 (2007).
13. Ni, X., Li, H., Liu, F. & Brédas, J.-L. Engineering of flat bands and Dirac bands in two-dimensional covalent organic frameworks (COFs): relationships among molecular orbital symmetry, lattice symmetry, and electronic-structure characteristics. *Mater. Horiz* **9**, 88-98 (2022).
14. Jiang, W., Ni, X. & Liu, F. Exotic topological bands and quantum states in metal-organic and covalent-organic frameworks. *Acc. Chem. Res.* **54**, 416-426 (2021).
15. Thomas, S., *et al.* Electronic structure of two-dimensional π -conjugated covalent organic frameworks. *Chem. Mater.* **31**, 3051-3065 (2019).
16. Springer, M. A., Liu, T.-J., Kuc, A. & Heine, T. Topological two-dimensional polymers. *Chem. Soc. Rev.* **49**, 2007-2019 (2020).
17. Baughman, R. H., Eckhardt, H. & Kertesz, M. Structure-property predictions for new planar forms of carbon: layered phases containing sp^2 and sp atoms. *J. Chem. Phys.* **87**, 6687-6699 (1987).
18. Haley, M. M., Brand, S. C. & Pak, J. J. Carbon networks based on dehydrobenzoannulenes: synthesis of graphdiyne substructures. *Angew. Chem. Int. Ed.* **36**, 836-838 (1997).
19. Huang, C. S., *et al.* Progress in research into 2D graphdiyne-based materials. *Chem. Rev.* **118**, 7744-7803 (2018).
20. Diederich, F. & Kivala, M. All-carbon scaffolds by rational design. *Adv. Mater.* **22**, 803-812 (2010).
21. Malko, D., Neiss, C., Vines, F. & Görling, A. Competition for graphene: graphynes with direction-dependent Dirac cones. *Phys. Rev. Lett.* **108**, 086804 (2012).
22. Clair, S. & de Oteyza, D. G. Controlling a chemical coupling reaction on a surface: tools and strategies for on-surface synthesis. *Chem. Rev.* **119**, 4717-4776 (2019).
23. Grill, L. & Hecht, S. Covalent on-surface polymerization. *Nat. Chem.* **12**, 115-130 (2020).
24. Barth, J. V., Costantini, G. & Kern, K. Engineering atomic and molecular nanostructures at surfaces. *Nature* **437**, 671-679 (2005).
25. Klappenberger, F., *et al.* On-surface synthesis of carbon-based scaffolds and nanomaterials using terminal alkynes. *Acc. Chem. Res.* **48**, 2140-2150 (2015).
26. Moreno, C., *et al.* Bottom-up synthesis of multifunctional nanoporous graphene. *Science* **360**, 199-203 (2018).
27. Galeotti, G., *et al.* Synthesis of mesoscale ordered two-dimensional π -conjugated polymers with semiconducting properties. *Nat. Mater.* **19**, 874-880 (2020).
28. Fan, Q., *et al.* Biphenylene network: a nonbenzenoid carbon allotrope. *Science* **372**, 852-856 (2021).
29. Grossmann, L., *et al.* On-surface photopolymerization of two-dimensional polymers ordered on the mesoscale. *Nat. Chem.* **13**, 730-736 (2021).
30. Zhang, Y. Q., *et al.* Homo-coupling of terminal alkynes on a noble metal surface. *Nature Communications* **3**, 1286 (2012).

31. Zhang, Y.-Q., *et al.* Synthesizing highly regular single-layer alkynyl–silver networks at the micrometer scale via gas-mediated surface reaction. *J. Am. Chem. Soc.* **141**, 5087–5091 (2019).
32. Zhang, Y.-Q., Björk, J., Barth, J. V. & Klappenberger, F. Intermolecular hybridization creating nanopore orbital in a supramolecular hydrocarbon sheet. *Nano Lett.* **16**, 4274–4281 (2016).
33. Yang, Z., *et al.* Two-dimensional delocalized states in organometallic bis-acetylide networks on Ag(111). *Nanoscale* **10**, 3769–3776 (2018).
34. Chen, Y. & Sun, Q. Magnetic two-dimensional organic topological insulator: Au-1,3,5-triethynylbenzene framework. *J. Chem. Phys.* **147**, (2017).
35. Yang, Z., *et al.* Metalated graphyne-based networks as two-dimensional materials: crystallization, topological defects, delocalized electronic states, and site-specific doping. *ACS Nano* **14**, 16887–16896 (2020).
36. Tetlow, H., *et al.* Growth of epitaxial graphene: theory and experiment. *Phys. Rep.* **542**, 195–295 (2014).
37. Auwärter, W. Hexagonal boron nitride monolayers on metal supports: versatile templates for atoms, molecules and nanostructures. *Surface Science Reports* **74**, 1–95 (2019).
38. Piquero-Zulaica, I., *et al.* Engineering quantum states and electronic landscapes through surface molecular nanoarchitectures. *Rev. Mod. Phys.* **94**, 045008 (2022).
39. Sperl, A., Kröger, J., Berndt, R., Franke, A. & Pehlke, E. Evolution of unoccupied resonance during the synthesis of a silver dimer on Ag(111). *New. J. Phys.* **11**, 063020 (2009).
40. Rizzo, D. J., *et al.* Revealing the local electronic structure of a single-layer covalent organic framework through electronic decoupling. *Nano Lett.* **20**, 963–970 (2020).
41. Offenbacher, H., *et al.* Orbital tomography: molecular band maps, momentum maps and the imaging of real space orbitals of adsorbed molecules. *J. Electron Spectrosc. Relat. Phenom.* **204**, 92–101 (2015).
42. Vasseur, G., *et al.* π band dispersion along conjugated organic nanowires synthesized on a metal oxide semiconductor. *J. Am. Chem. Soc.* **138**, 5685–5692 (2016).
43. Udhardt, C., *et al.* π -like band structure observed for coronene monolayers deposited on Ag(111). *J. Electron Spectrosc. Relat. Phenom.* **227**, 40–43 (2018).
44. Feng, B., *et al.* Discovery of Weyl nodal lines in a single-layer ferromagnet. *Phys. Rev. Lett.* **123**, 116401 (2019).
45. Hohenberg, P. & Kohn, W. Inhomogeneous electron gas. *Phys. Rev.* **136**, B864–B871 (1964).
46. Paolo, G., *et al.* QUANTUM ESPRESSO: a modular and open-source software project for quantum simulations of materials. *J. Phys.: Condens. Matter* **21**, 395502 (2009).
47. Hamada, I. van der Waals density functional made accurate. *Phys. Rev. B* **89**, (2014).
48. Blöchl, P. E. Projector augmented-wave method. *Phys. Rev. B* **50**, 17953–17979 (1994).
49. Tersoff, J. & Hamann, D. R. Theory of the scanning tunneling microscope. *Phys. Rev. B* **31**, 805–813 (1985).

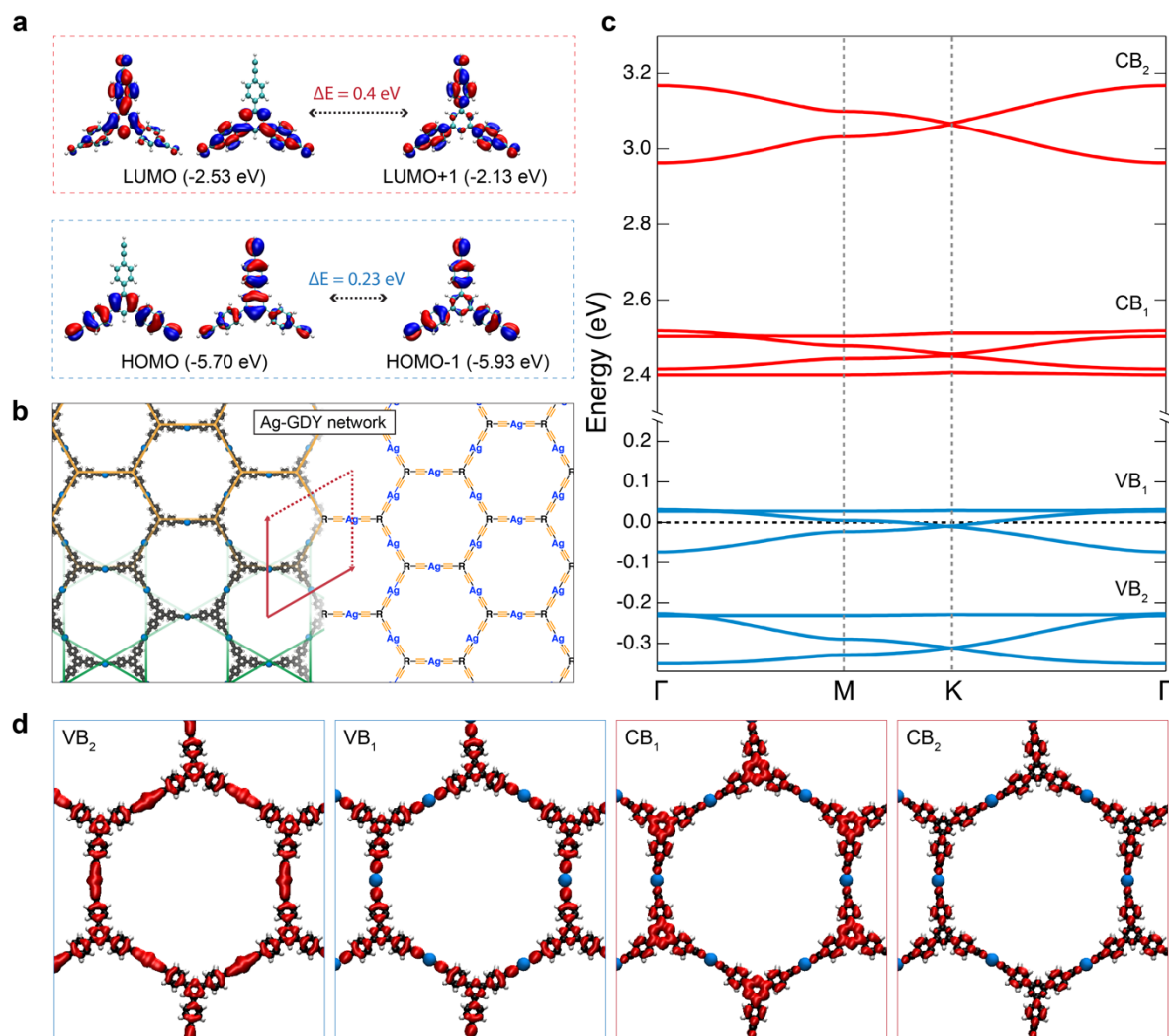


Fig. 1 | Doubly degenerate precursor LUMO and HOMO account for flat, Dirac and Kagome bands in the Ag-GDY sheet. a, DFT calculated frontier molecular orbitals of isolated Ext-TEB molecule. **b**, Model and chemical scheme of freestanding Ag-GDY sheet with rhombic unit cell. Honeycomb and Kagome lattices occupied by molecules and Ag atoms are highlighted, respectively. **c**, Band structure around the Fermi level and above the band gap of the freestanding network. Red and blue colours are used to distinguish CBs and VBs. **d**, Integrated network orbital density of the first and second groups of VBs and CBs, respectively.

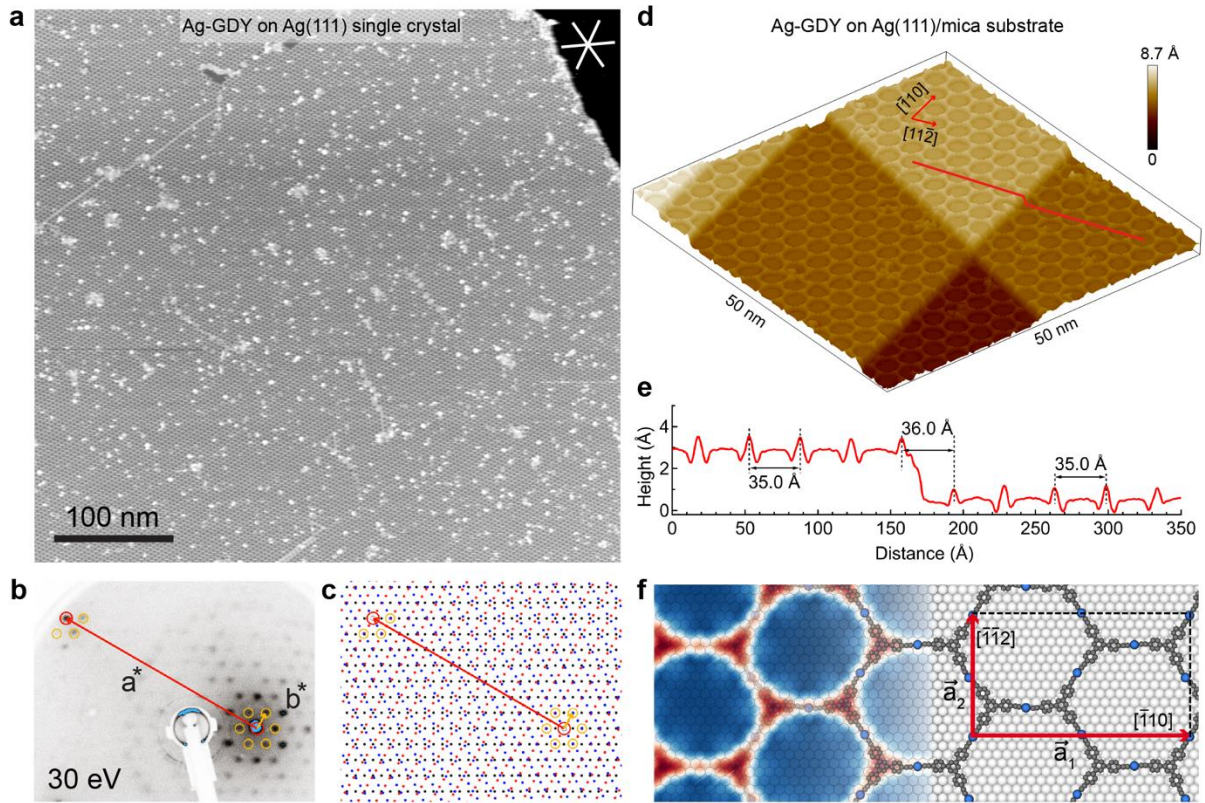


Fig. 2 | Overview STM images of Ag-GDY network grown on Ag(111) facets. **a**, STM image of a continuous $500 \times 500 \text{ nm}^2$ atomically thin Ag-GDY network grown on an Ag(111) single crystal. $I_t = 100 \text{ pA}$, $U_b = -1.0 \text{ V}$. **b**, LEED pattern of Ag-GDY/Ag(111) for $T_{\text{sub}} = 90 \text{ K}$ and $E_{\text{electron}} = 30 \text{ eV}$. **c**, Modelling of the LEED pattern. **d**, 3D rendering of an STM image showing the continuity of the network crossing straight steps on Ag(111)/mica. $I_t = 50 \text{ pA}$, $U_b = 0.1 \text{ V}$. **e**, STM contour of line marked in (**d**). **f**, Structure model of Ag-GDY network with rectangular unit cell on Ag(111) facet.

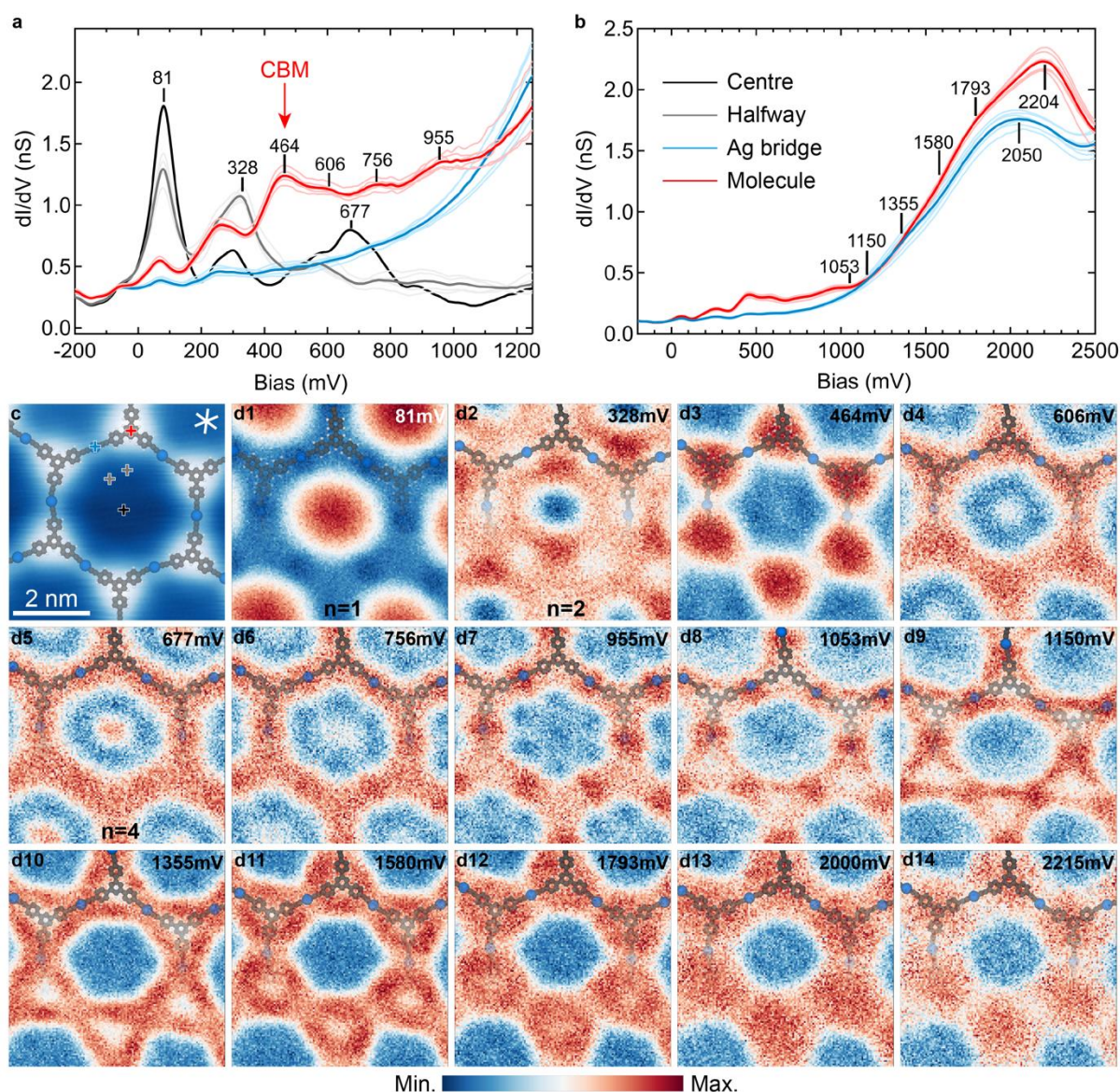


Fig. 3 | STS characterization of the elementary constituent in a Ag-GDY/Ag(111) sheet.

a-b, Site-specific dI/dV spectra taken in the bias range from -0.2 to 1.2 V and extended bias range from -0.3 to 2.5 V, respectively. Set point: $I_t = 50$ pA, $U_b = -0.2$ V and -0.3 V, $U_m = 20$ mV. **c,** Corresponding STS survey area in the network, superimposed with a DFT model with rectangular unit cell. $I_t = 50$ pA, $U_b = 0.96$ V. **d,** Bias-dependent dI/dV mapping of the regular six-membered ring shown in (c). Set point: $I_t = 50$ pA, $U_m = 20$ mV.

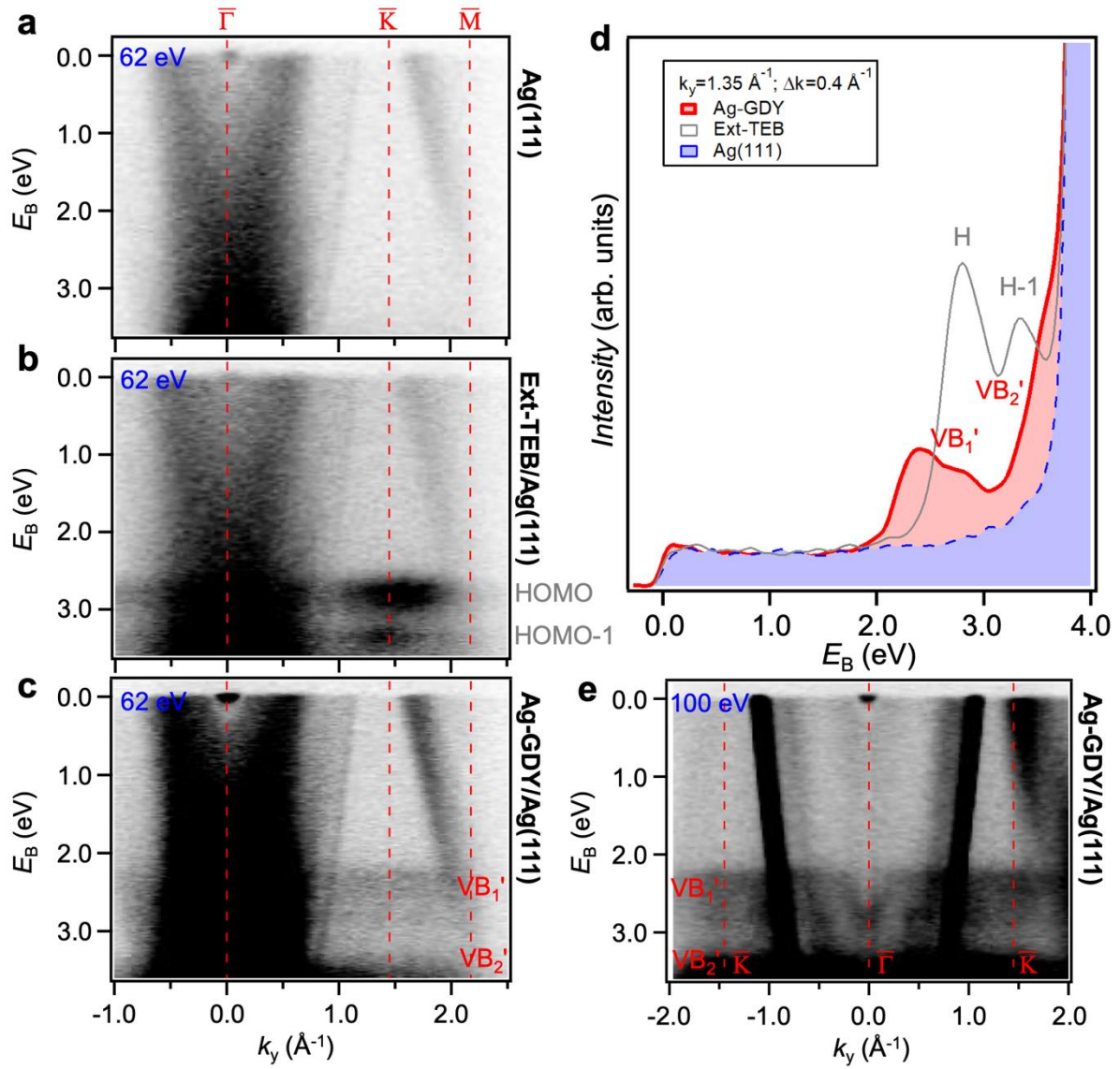


Fig. 4 | Evolution of ARPES band structure upon Ag-GDY sheet formation. **a-c**, Band structure (E_B vs. k_y) of pristine Ag(111), Ext-TEB organic multilayer and Ag-GDY network measured along the $[1\bar{1}0]$ substrate direction (i.e. along $\bar{\Gamma}\bar{K}$) with a photon energy of 62 eV. **d**, EDCs at $k_y = 1.35 \text{ \AA}^{-1}$ evidence discrete occupied frontier orbitals for pure Ext-TEB molecules and their transformation to a valence band (VB_1' with a ~ 0.8 eV bandwidth) upon Ag-GDY network formation. The additional onset close to the Ag d -bands corresponds to the VB_2' . **e**, Same band structure as in (c) measured with 100 eV photon energy: While Ag- sp bands shift with photon energy, the Ag-GDY bands remain unchanged in accordance with their 2D nature. ARPES experimental datasets in (a) and (b) were obtained at RT, (c) and (e) at $T \approx 60$ K.

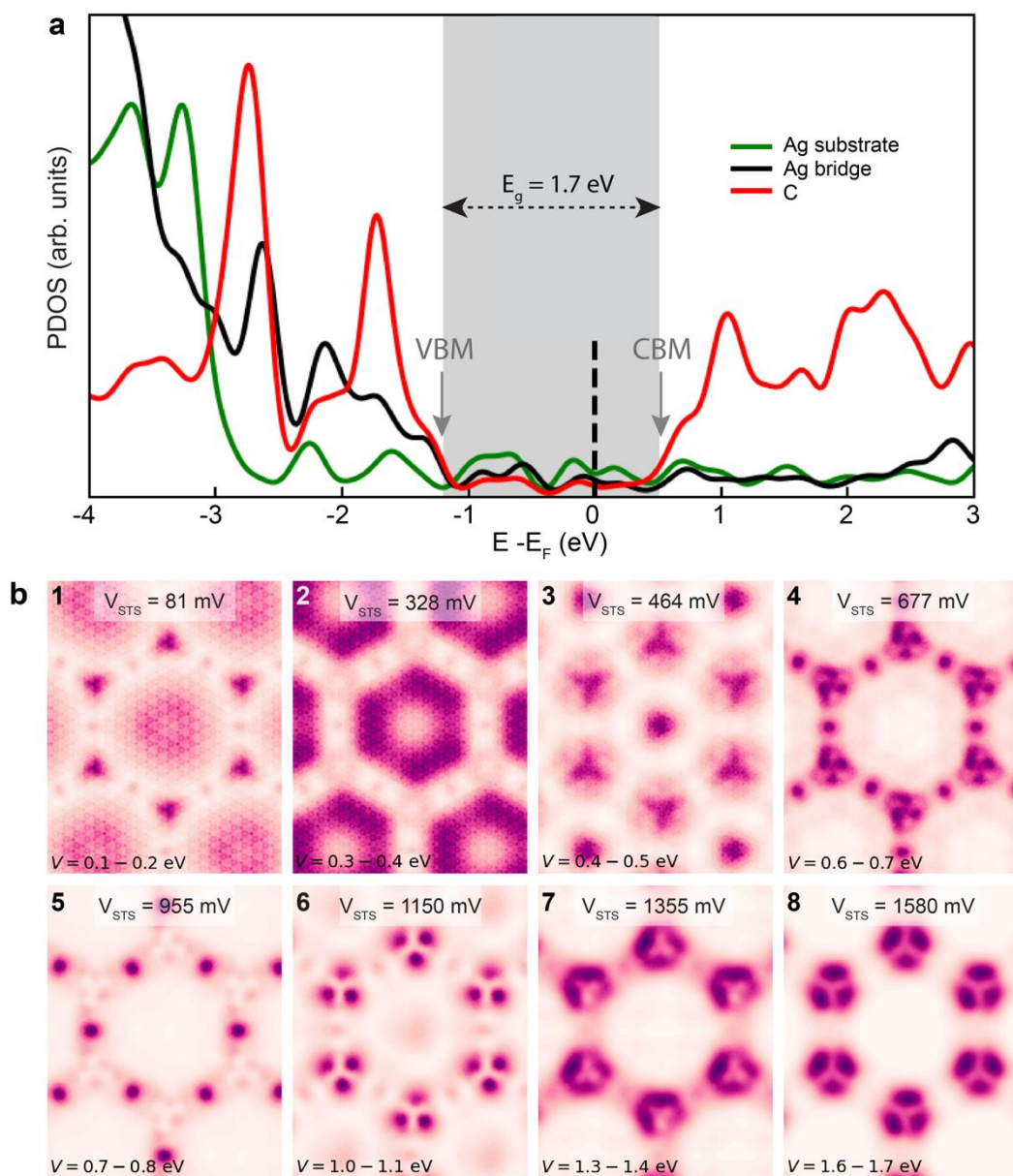


Fig. 5 | DFT modelization of Ag-GDY/Ag(111) electronic features. **a**, Projected DOS of the Ag-GDY network adsorbed on four-layer Ag(111) slab. Contributions from carbon, alkynyl-Ag atoms and substrate are distinguished by different colours. **b**, Simulated dI/dV maps with characteristic LDOS patterns corresponding to the experimental bias values, indicated on the top of individual figures.

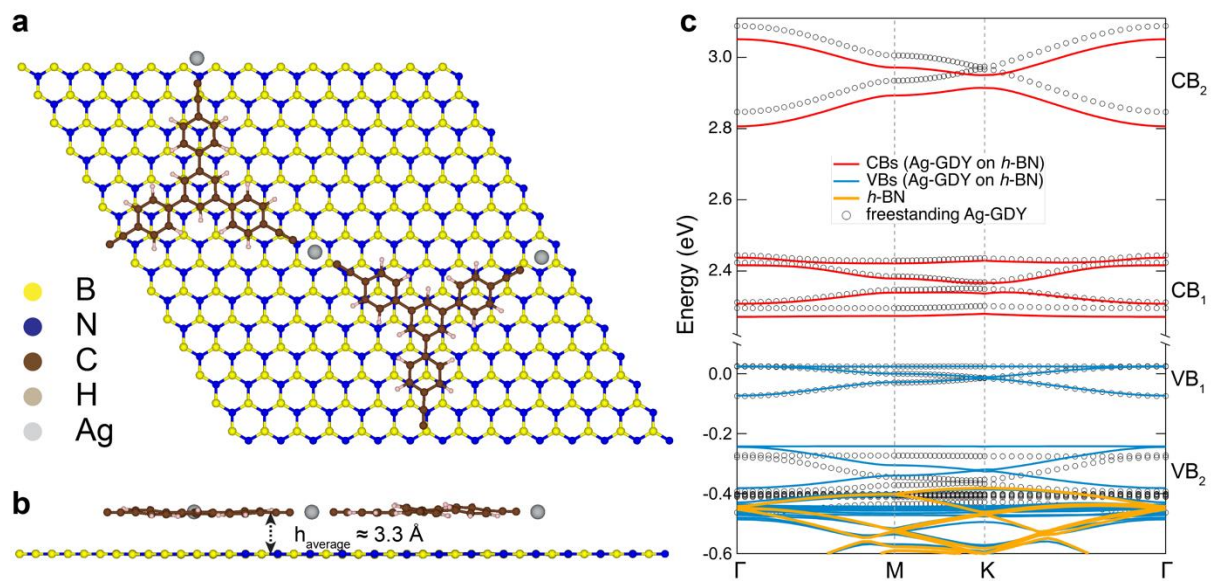


Fig. 6 | DFT calculated band structure of Ag-GDY sheet on *h*-BN. **a-b**, Top and side views of the large Ag-GDY/*h*-BN unit cell with averaged adsorption height indicated. **c**, Band structure of Ag-GDY/*h*-BN (red and blue solid lines) compared with freestanding Ag-GDY (black circles) with same geometry adopted from the combined system shown in (a). *h*-BN bands are highlighted in orange.

SUPPLEMENTARY INFORMATION

Unconventional band structure via combined molecular orbital and lattice symmetries in a surface-confined metallated graphdiyne sheet

Ignacio Piquero-Zulaica^{1,†,*}, Wenqi Hu^{2,†}, Ari Paavo Seitsonen^{3,†}, Felix Haag¹, Johannes K  chle¹, Francesco Allegretti¹, Yuanhao Lyu², Lan Chen², Kehui Wu², Zakaria M. Abd El-Fattah⁴, Ethem Akt  rk⁵, Svetlana Klyatskaya⁶, Mario Ruben^{6,7}, Matthias Muntwiler⁸, Johannes V. Barth^{1,*} and Yi-Qi Zhang^{2,1*}

¹*Physics Department E20, Technical University of Munich, D-85748 Garching, Germany*

²*Institute of Physics, Chinese Academy of Sciences, 100190 Beijing, China*

³*D  partement de Chimie,   cole Normale Sup  rieure, 24 rue Lhomond, F-75005 Paris, France*

⁴*Physics Department, Faculty of Science, Al-Azhar University, Nasr City, E-11884, Cairo, Egypt*

⁵*Department of Physics, Adnan Menderes University, 09100 Aydin, Turkey*

⁶*Institute of Nanotechnology, Karlsruhe Institute of Technology, 76344 Eggenstein-Leopoldshafen, Germany*

⁷*IPCMS-CNRS, Universit   de Strasbourg, 23 rue de Loess, 67034 Strasbourg, France*

⁸*Paul Scherrer Institute, Forschungsstrasse 111, 5232 Villigen PSI, Switzerland*

†These authors contributed equally.

*Email: ge46biq@mytum.de; jvb@tum.de; yiqi.zhang@iphy.ac.cn

Index

Supplementary Figure 1:

Band structure of the freestanding Ag-GDY sheet

Supplementary Figure 2:

DFT-calculated molecular orbitals of gas-phase Ext-TEB

Supplementary Figure 3:

Large-scale STM images of Ag-GDY networks on Ag(111) single-crystal surface

Supplementary Figure 4:

LEED pattern modelling of the Ag-GDY network on Ag(111) single-crystal surface

Supplementary Figure 5:

The continuity of the Ag-GDY networks at the step edges

Supplementary Figure 6:

Modelling of the network distortion at step edge

Supplementary Figure 7:

Rectangular unit cell of Ag-GDY network grown on the Ag(111)/mica substrate

Supplementary Figure 8:

dI/dV characterization of discrete and disordered organometallic network

Supplementary Figure 9:

Larger-scale dI/dV maps of the Ag-GDY network

Supplementary Figure 10:

Larger-scale images of the Kagome electronic grid

Supplementary Figure 11:

dI/dV point spectra of Ag-GDY network at occupied regime

Supplementary Figure 12:

LEED characterization of pristine and Ag-GDY covered Ag(111) surface

Supplementary Figure 13:

ARPES characterization of the clean Ag(111) crystal

Supplementary Figure 14:

ARPES characterization of a thin Ext-TEB multilayer on Ag(111)

Supplementary Figure 15:

ARPES band structure in second derivative comparing Ag(111), Ext-TEB/Ag(111) and Ag-GDY/Ag(111)

Supplementary Figure 16:

Ag-GDY ARPES band structure dependence with photon energy

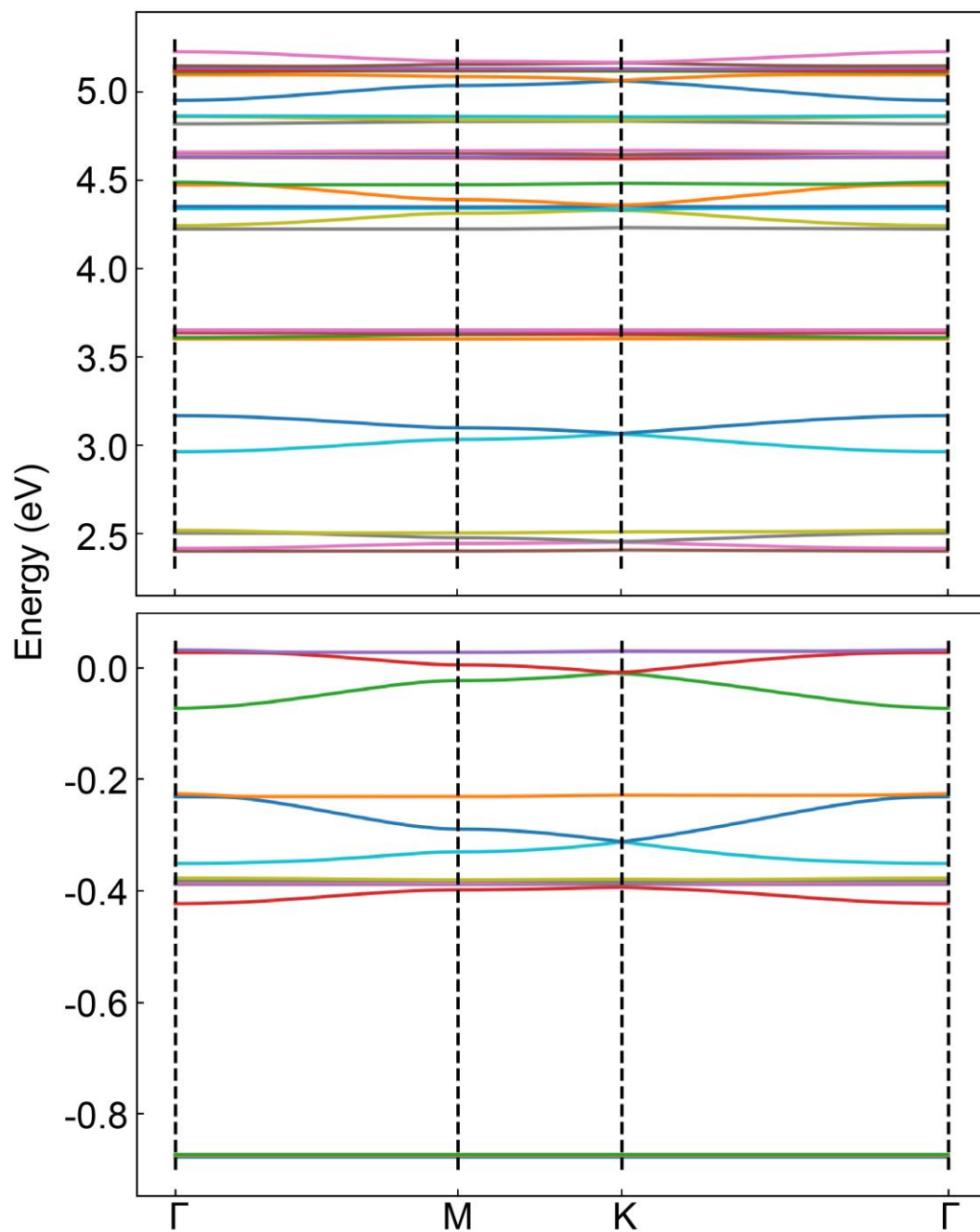
Supplementary Figure 17:

DFT-calculated nanopore-confined surface states

Supplementary Figure 18-20:

DFT-calculated projected band structure and DOS of freestanding and adsorbed Ag-GDY

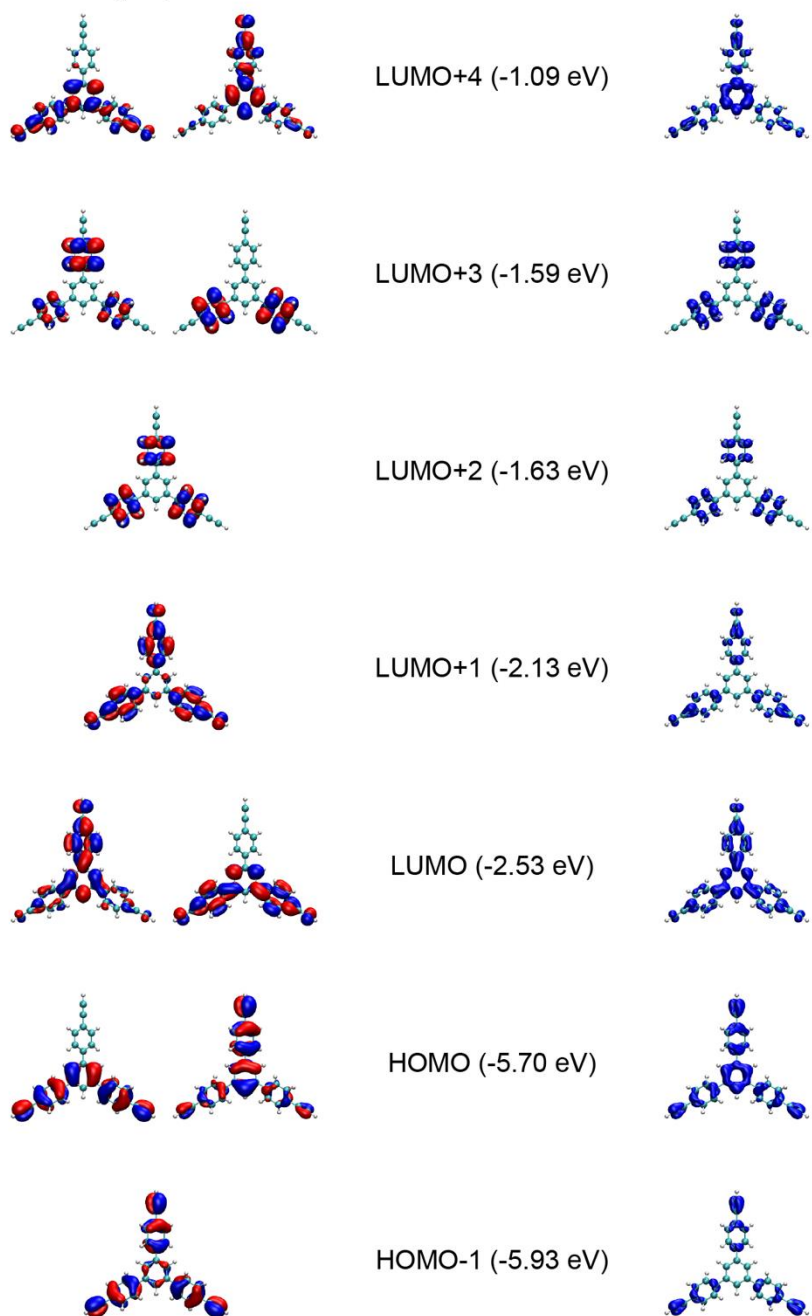
References



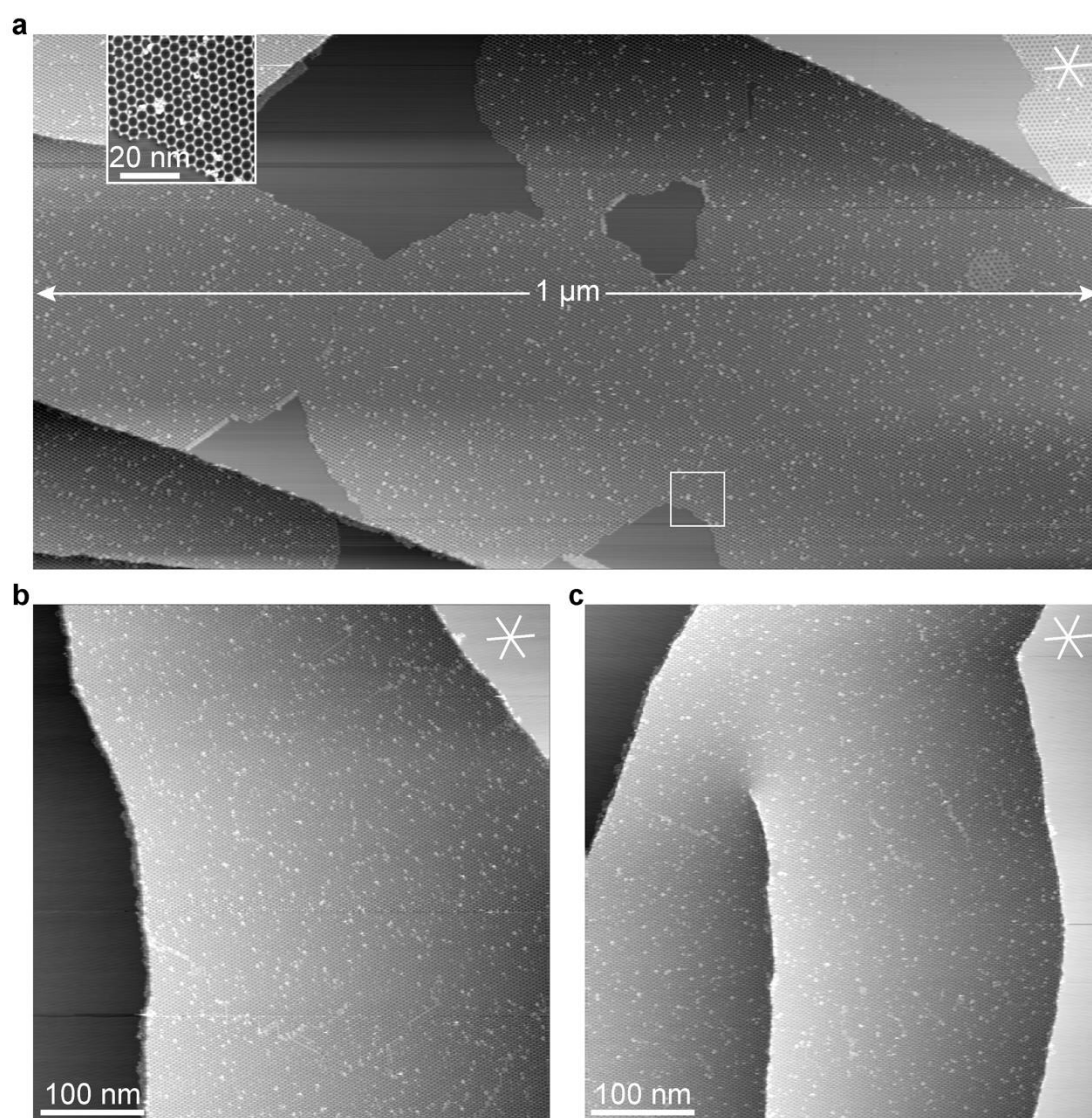
Supplementary Figure 1 | Band structure of the freestanding Ag-GDY sheet. The network geometry is adopted from the relaxed system with four-layer-Ag-slab, where a rhombic unit cell is employed.

Orbitals of a gas-phase Ext-TEB

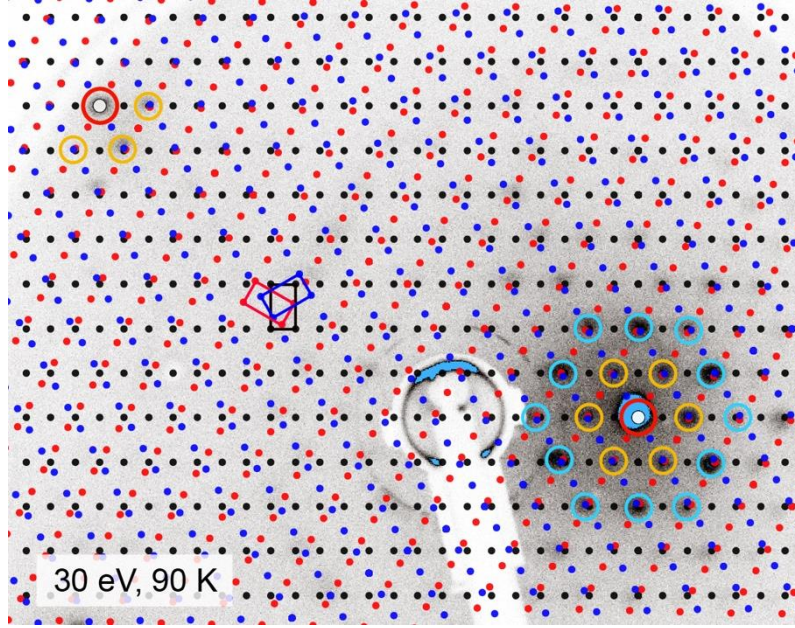
Orbital densities



Supplementary Figure 2 | DFT-calculated molecular orbitals of gas-phase Ext-TEB.

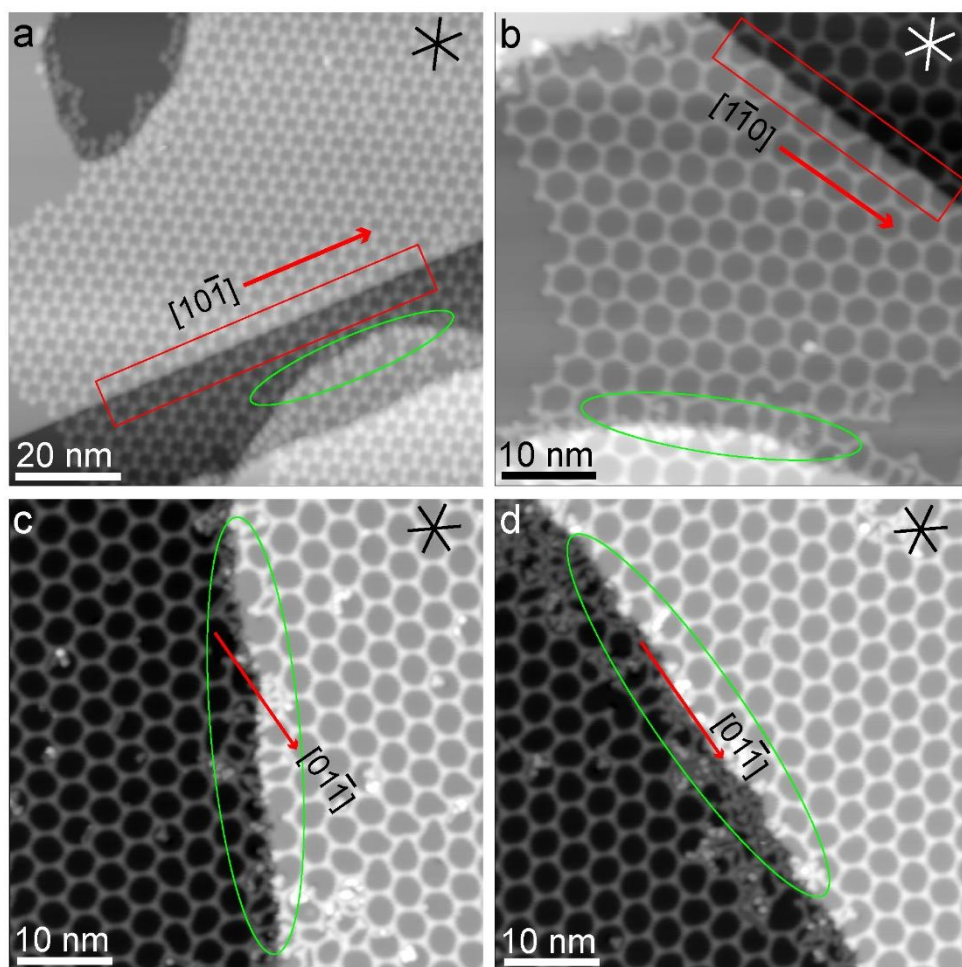


Supplementary Figure 3 | Large-scale STM images of single-domain Ag-GDY networks grown on large terraces of the Ag(111) single-crystal surface. Scanning parameters: (a) $I_t = 100$ pA, $U_b = -1$ V. Inset: $I_t = 100$ pA, $U_b = -100$ mV. (b) $I_t = 100$ pA, $U_b = -1$ V. (c) $I_t = 100$ pA, $U_b = -100$ mV. The bright protrusions in the networks correspond to impurities as well as trapped molecules¹.



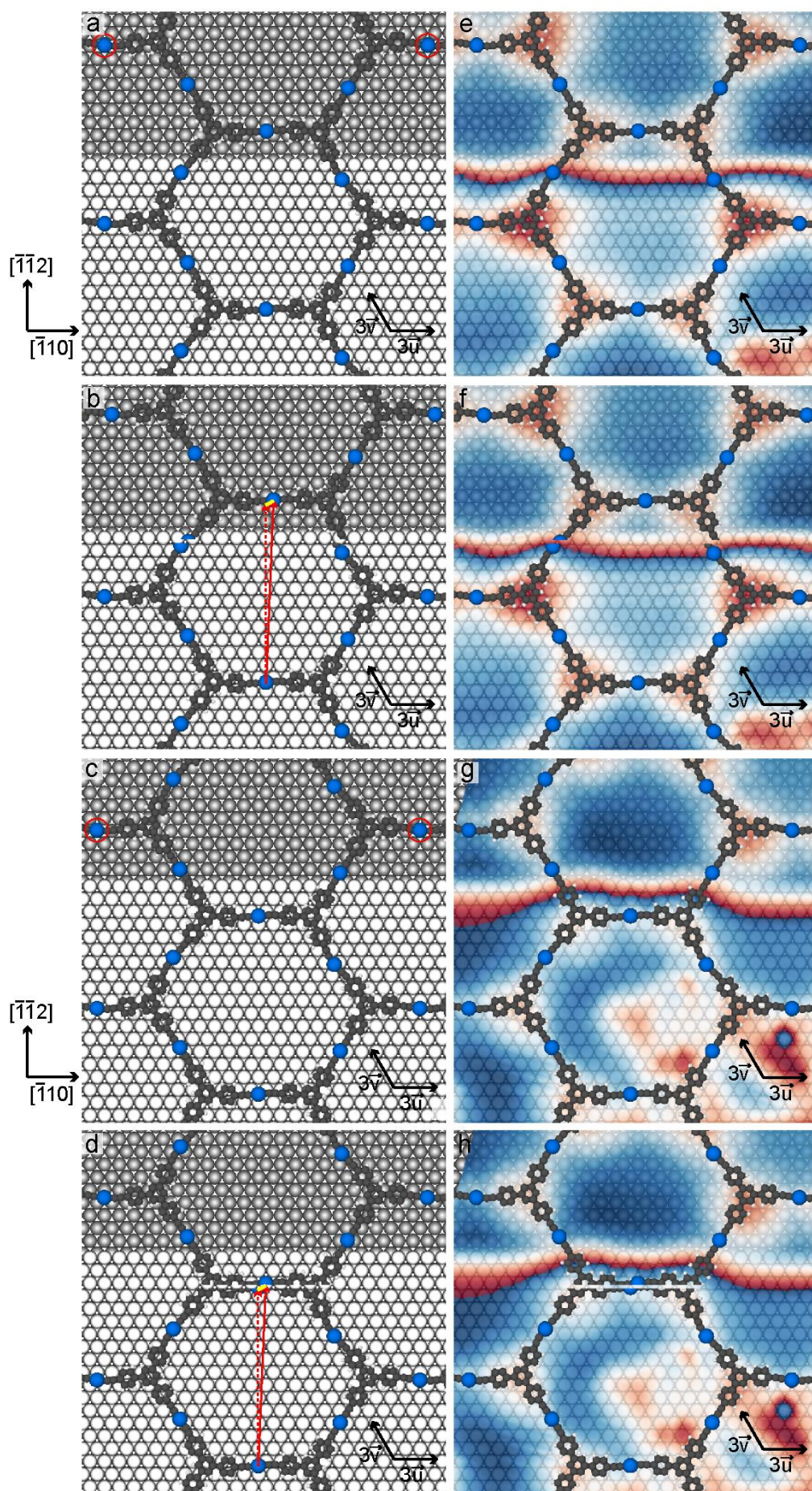
Supplementary Figure 4 | LEED pattern modelling. LEED pattern of the Ag-GDY sheet prepared on the Ag(111) single-crystal surface. $T_{\text{meas}} = 90 \text{ K}$, $E_{\text{electron}} = 30 \text{ eV}$. The overlayer is simulated LEED pattern generated using the *LEEDpat* software. Three sets of equivalent lattices are distinguished using red, blue and black dots, respectively. Red circles mark the diffraction spots of Ag(111). Yellow and blue circles highlight the first and the second order diffraction spots of the Ag-GDY network, respectively.

Simulated LEED pattern was generated via the *LEEDpat* software (<http://www.fhi-berlin.mpg.de/KHsoftware/LEEDpat/>) using the experimentally determined rectangular-unit-cell parameters¹. Three equivalent domains with a rotation angle of 120° are taken into account. Ag(111) diffraction spots (red circles) are used for calibrating the simulated LEED pattern to be compared with the experimental LEED photo. It is clear to see that the first (yellow circles) and second (light blue circles) order diffraction spots correspond to the reciprocal spots where three sublattices present the maximum overlap.



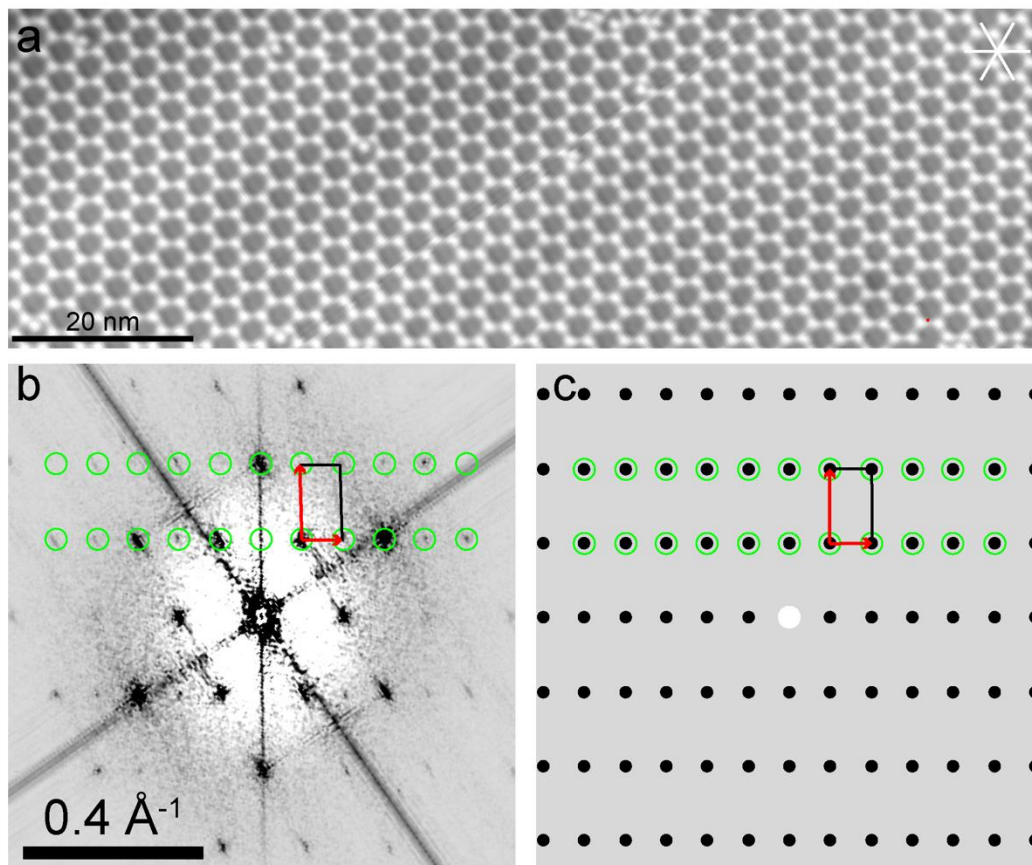
Supplementary Figure 5 | The continuity of the Ag-GDY network at the step edges. (a,b) STM images of Ag-GDY network growing continuously across a monoatomic-height step along the high symmetry direction on the Ag(111)/mica substrate. (c,d) STM images of Ag-GDY networks discontinued at the monoatomic-height step edges on the Ag(111) single-crystal surface. Solid red rectangles highlight atomically straight step edges. Green ellipses highlight irregular step edges. High-symmetry directions of all the Ag(111) surfaces are indicated. Scanning parameters: (a) $I_t = 30$ pA, $U_b = 1$ V; (b) $I_t = 50$ pA, $U_b = 0.5$ V; (c, d) $I_t = 100$ pA, $U_b = -1$ V.

On the Ag(111)/mica substrate, there exhibits atomically-sharp step edges along high symmetry directions, and we found that Ag-GDY network can grow continuously across such a monoatomic-height step (cf. also Fig. 2d in the main text). We found that the network is slightly stretched (3%) along the direction perpendicular to the step edge (Supplementary Fig. 6).



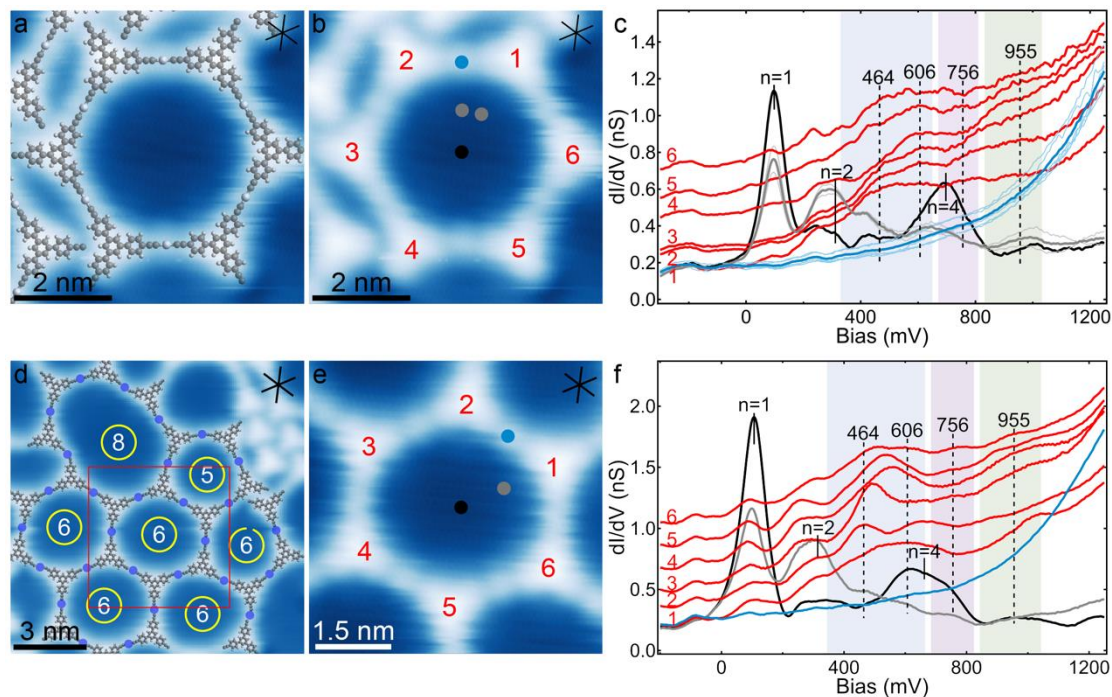
Supplementary Figure 6 | Modelling of network distortion at step edge. Two different adsorption geometries are analysed. Alkynyl-Ag atoms (a) or Ext-TEB molecules (c) are locating at the step edge with favourable network adsorption configuration on the upper terrace. The red circles highlight the alkynyl-Ag atom sitting on the top site. (b,d) Ideal network adsorption configurations on both terraces with a small shear present at the step edge. The red dotted and solid-line vectors show the alkynyl-Ag position before and after a small displacement, indicated by the yellow line. Four different models shown in (a-d) are superimposed with STM images and displayed in (e-h).

The adsorption registry for the Ag-GDY network growing continuously across step edge is modelled based on DFT-relaxed structure on the flat surface¹. Supplementary Fig. 6 shows two types of step-crossing geometries, with alkynyl-Ag atom (Supplementary Fig. 6a) or Ext-TEB molecule (Supplementary Fig. 6c) locating at the step edge, respectively. If we assume that there exhibits a stretching vector $\frac{2}{3}\vec{u} + \frac{1}{3}\vec{v}$ (Supplementary Fig. 6b,d) at the step edge, all alkynyl-Ag adatoms on both terraces can be assigned to the Ag(111) hollow sites, i.e., on the favourable adsorption sites. Note that the stretching projection along the $[\bar{1}\bar{1}2]$ direction is $\sim 0.3a_0$ ($a_0=2.889$ Å), which agrees well the experimental data (~ 1 Å) as shown in Fig. 2e in the main text.

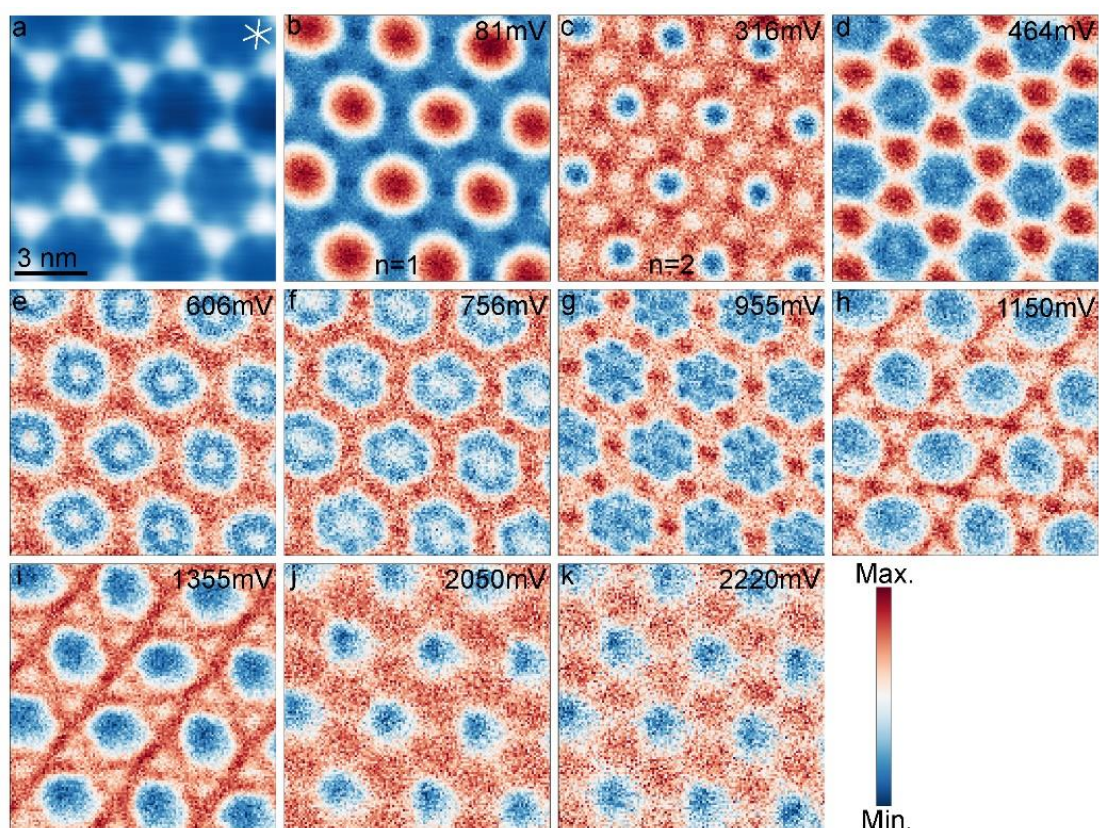


Supplementary Figure 7 | Rectangular unit cell of Ag-GDY network grown on the Ag(111)/mica substrate. (a) STM image of a single domain of the Ag-GDY network grown on the Ag(111)/mica substrate. High-symmetry directions of the Ag(111)/mica surface are indicated. $I_t = 30$ pA, $U_b = 1.0$ V. (b) The 2D fast Fourier transform (2D-FFT) of an area ($120\text{ nm} \times 120\text{ nm}$). (c) The simulated LEED pattern of a single domain of the Ag-GDY network. Green cycles highlight rectangular reciprocal lattice of the network. The white dot denotes the reciprocal lattice spot of Ag(111).

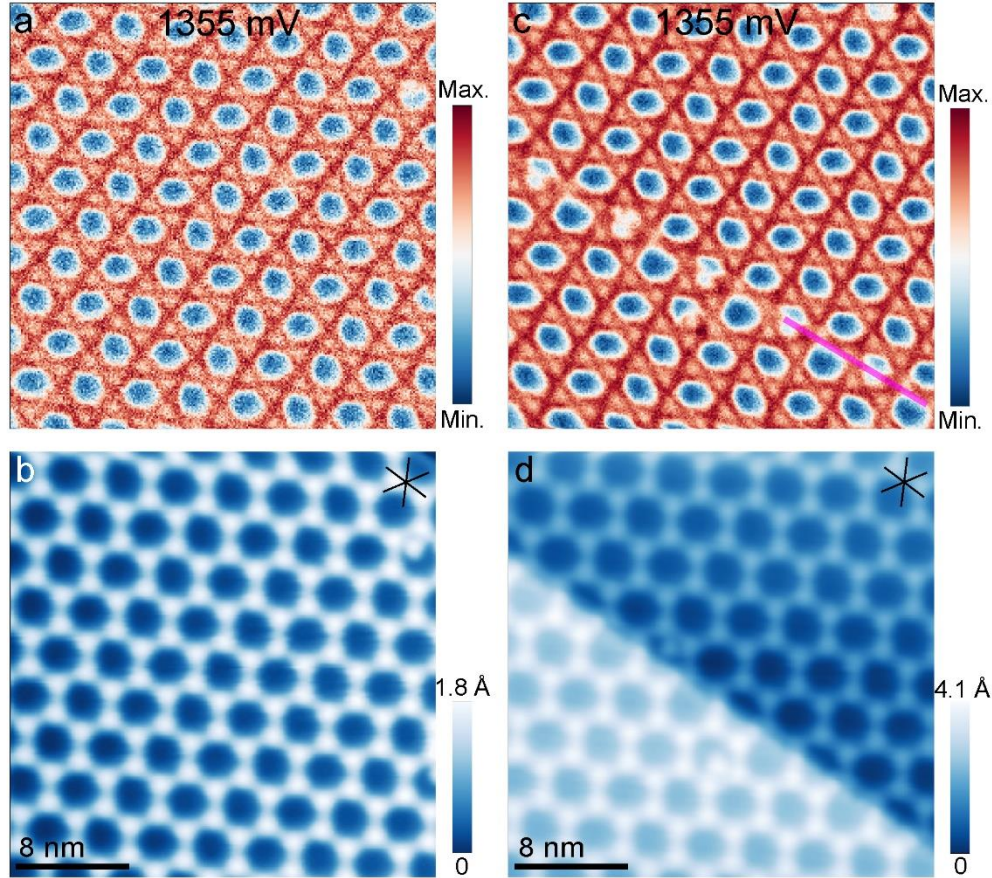
Supplementary Figure 7a is an STM overview image of a single domain of the Ag-GDY network grown on the Ag(111)/mica substrate. We can obtain a commensurate rectangular unit cell ($a_1 = 63.6\text{ Å}$, $a_2 = 35.0\text{ Å}$), which agrees well with our previous result¹. The periodic rectangular reciprocal lattice shown in 2D-FFT image (cf. Supplementary Fig. 7b) obtained from a large single domain corroborates the rectangular unit cell and agrees with the simulated reciprocal lattice employing the *LEEDpat* software.



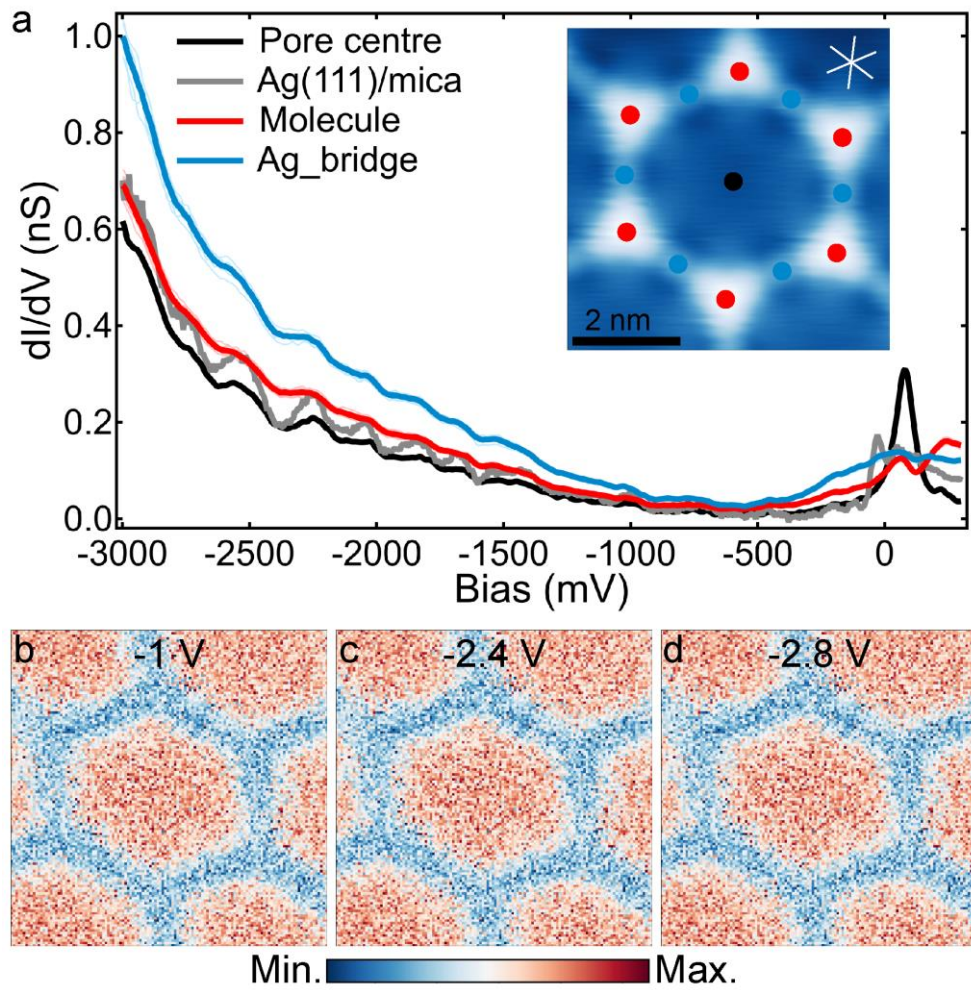
Supplementary Figure 8 | dI/dV characterization of discrete and disordered organometallic network on Ag(111)/mica. High-resolution STM image of a six-membered organometallic ring superimposed with the model (a) and point-spectra sites (b). (c) Site-dependent dI/dV spectra of the organometallic hexamer. Set point: $I_t = 50$ pA, $U_b = -300$ mV, $U_m = 20$ mV. (d) STM image of a disordered network. Yellow cycles and numbers highlight the surrounding numbers of the molecules. (e) Magnified STM image of (d) with six-membered ring embedded in the disordered network with point-spectra sites indicated and corresponding dI/dV spectra displayed in (f). Set point: $I_t = 50$ pA, $U_b = -200$ mV, $U_m = 20$ mV.



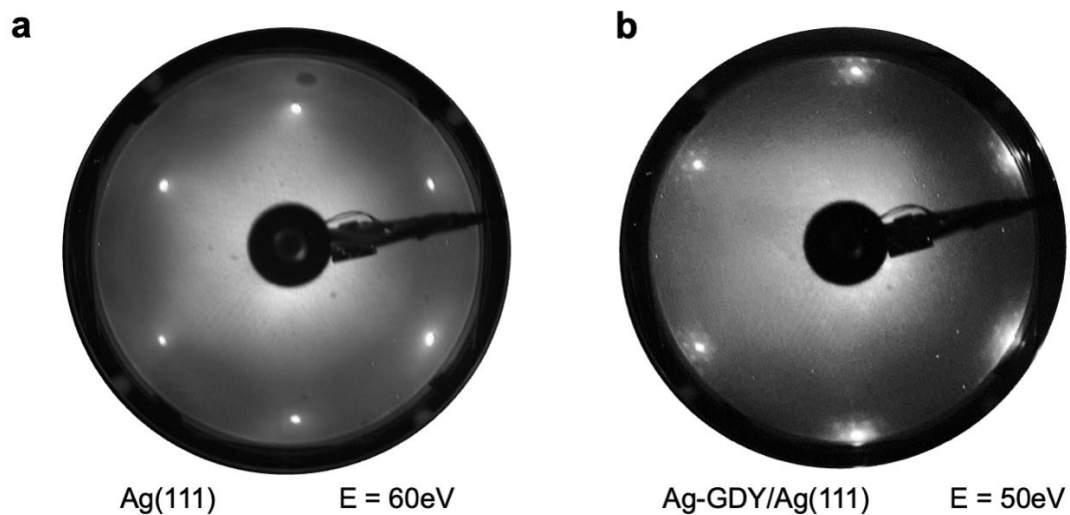
Supplementary Figure 9 | Larger-scale dI/dV maps of the Ag-GDY network at the unoccupied regime. (a) Larger-scale STM image of Ag-GDY network. $I_t = 50$ pA, $U_b = 606$ mV. High-symmetry directions of the Ag(111)/mica surface are indicated. (b-k) Corresponding dI/dV maps at different bias voltages. Set point: $I_t = 50$ pA, $U_m = 20$ mV.



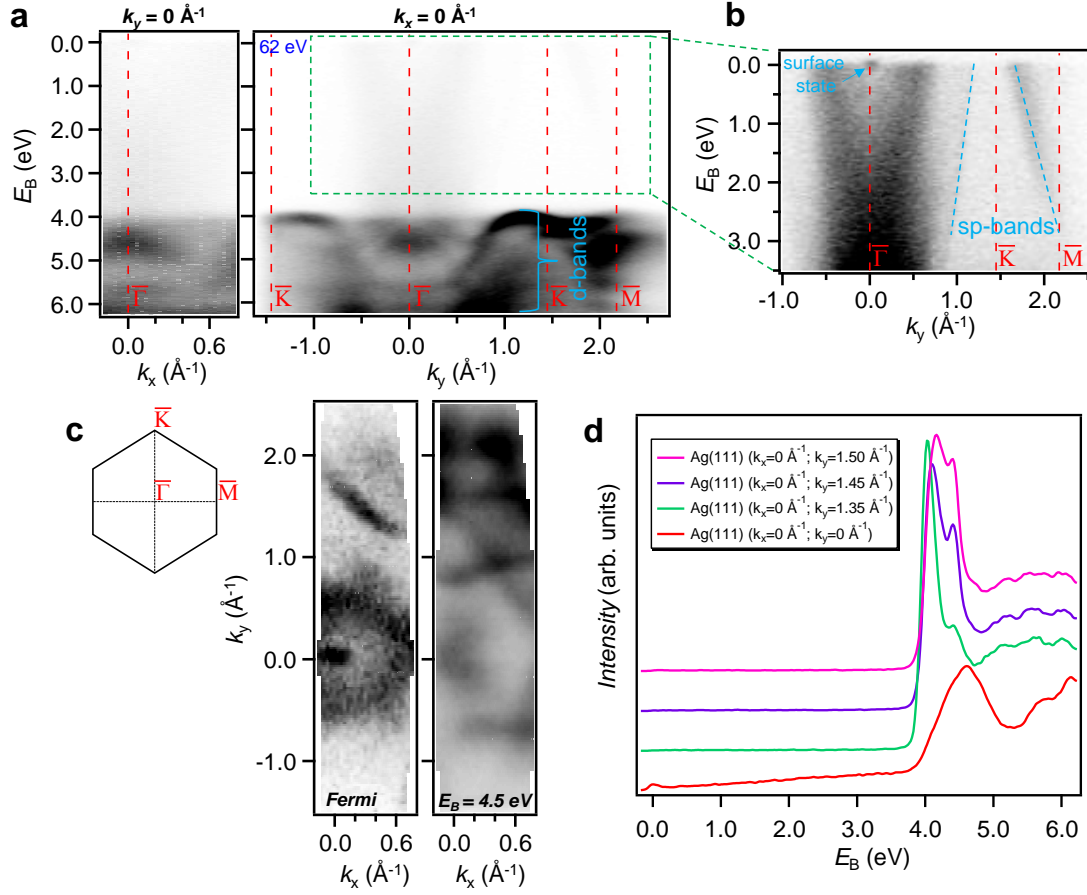
Supplementary Figure 10 | Larger-scale images of the Kagome electronic grid. (a) Larger-scale ($30 \text{ nm} \times 30 \text{ nm}$) dI/dV map of real-space Kagome electronic grid at 1355 mV, distributed homogeneously on the entire Ag-GDY network. Set point: $I_t = 50 \text{ pA}$, $U_m = 20 \text{ mV}$. (b) Corresponding STM image of (a). Set point: $I_t = 50 \text{ pA}$, $U_b = 1.355 \text{ V}$. (c) Kagome electronic grid, which is continuous at atomically straight and monoatomic-height step at 1355 mV. Set point: $I_t = 50 \text{ pA}$, $U_m = 20 \text{ mV}$. (d) Corresponding STM image of (c). Set point: $I_t = 50 \text{ pA}$, $U_b = 1.355 \text{ V}$. High-symmetry directions of the Ag(111)/mica surface are indicated.



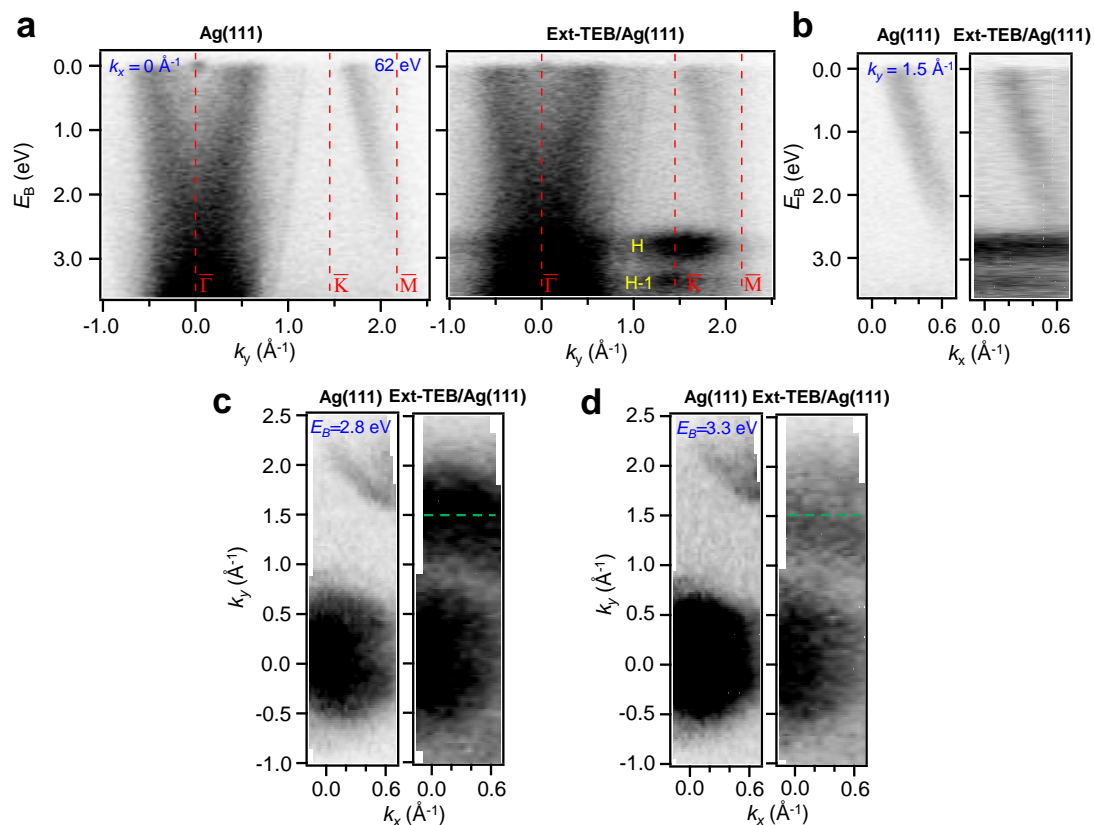
Supplementary Figure 11 | dI/dV point spectra of Ag-GDY network at occupied regime. (a) Site-dependent dI/dV spectra of a single hexagonal constituent of Ag-GDY network. The LDOS is featureless below Fermi energy. Set point: $I_t = 30$ pA, $U_b = 0.30$ V, $U_m = 20$ mV. Inset, $I_t = 30$ pA, $U_b = 300$ mV. (b-d) dI/dV maps of a single pore at selected bias voltages. Set point: $I_t = 50$ pA, $U_m = 20$ mV.



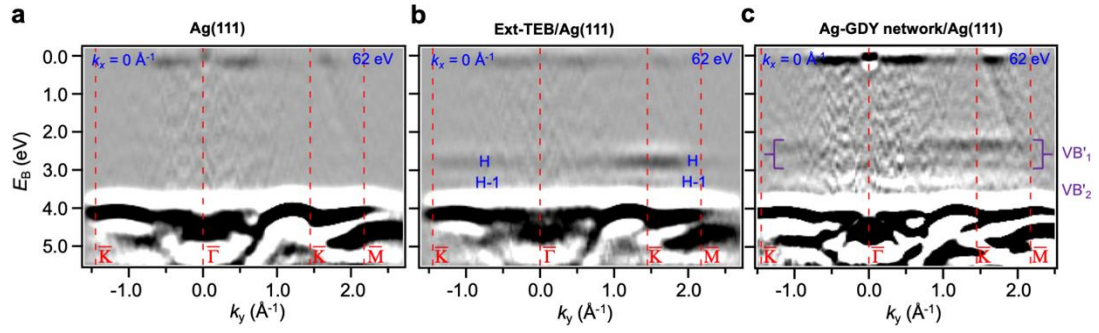
Supplementary Figure 12 | LEED pattern comparison between pristine Ag(111) and Ag-GDY network fully covered Ag(111) surface during ARPES characterization. (a) LEED pattern obtained for the pristine Ag(111) surface at 60 eV. (b) LEED pattern corresponding to the Ag-GDY network fully covered Ag(111) surface obtained at 50 eV. The diffraction pattern is identical to the one shown in Fig. 2b in the main text.



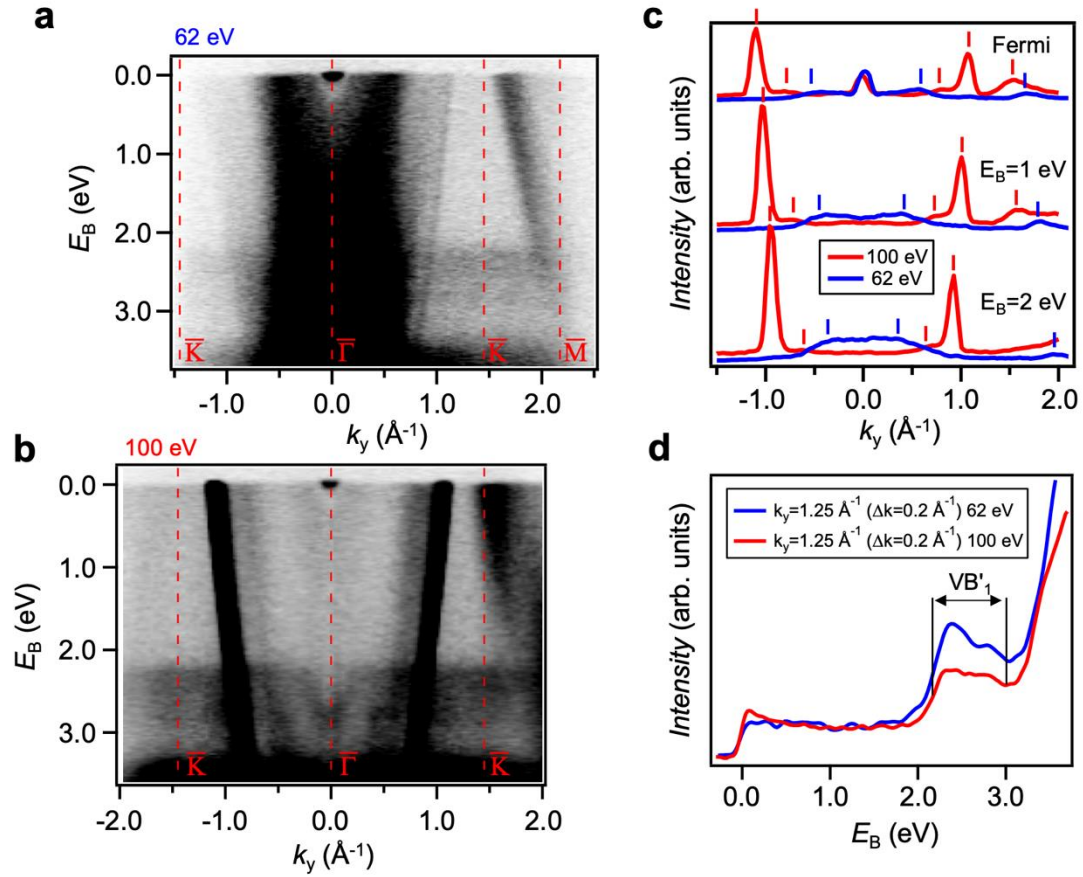
Supplementary Figure 13 | Electronic structure of the Ag(111) crystal. (a) ARPES band structure (E vs k_x at $k_y=0 \text{ \AA}^{-1}$) (left) and (E vs k_y at $k_x=0 \text{ \AA}^{-1}$) (right), corresponding to the direction parallel to the $[11\bar{2}]$ and $[1\bar{1}0]$ respectively. The characteristic silver d -bands appear below 4 eV. (b) A closer inspection into the valence band reveals the characteristic parabolic Ag surface state at the $\bar{\Gamma}$ point and the dispersive character of the sp -bands, as they raise and cross the Fermi level (highlighted by a side dashed light blue line). (c) Fermi surface map (k_x vs k_y at $E=0 \text{ eV}$) (left) and at $E=4.5 \text{ eV}$ (right), exhibiting the isotropic Ag surface state close to the $\bar{\Gamma}$ point, the dispersive dominant sp -bands close to the \bar{K} point and the hexagonal shape of the d -bands. At 62 eV photon energy, an additional spectral intensity is captured at $\bar{\Gamma}$ stemming from the projection of bulk bands. (d) Energy distribution curves (EDCs) extracted at different k_y values along the $\bar{\Gamma}\bar{K}$ direction. They clearly portray the Ag surface state and intensity from the projected bulk bands at $\bar{\Gamma}$ along with the highly intense onset of the d -bands beyond 4 eV.



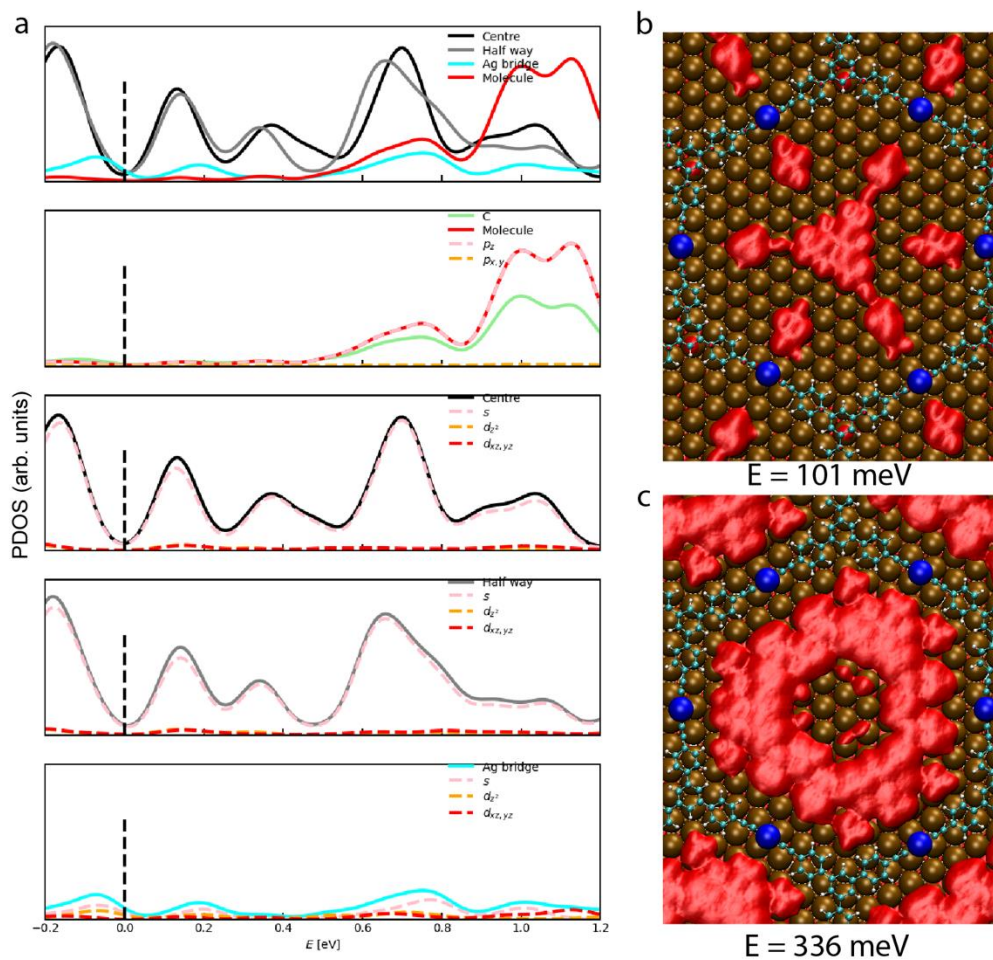
Supplementary Figure 14 | ARPES band structure comparison between pristine Ag(111) and intact Ext-TEB multilayer on Ag(111). (a) ARPES band structure (E vs k_y at $k_x = 0 \text{ \AA}^{-1}$) along the $[1\bar{1}0]$ direction for the pristine Ag (left) and intact Ext-TEB multilayer (right). Localized frontier molecular orbitals named as HOMO (H) and HOMO-1 (H-1) appear at the characteristic wave-vector of $k_y = 1.5 \text{ \AA}^{-1}$. (b) The orthogonal ARPES band structure (E vs k_x at $k_y = 1.5 \text{ \AA}^{-1}$) clearly evidences the lack of dispersion of the H and H-1. (c) Isoenergetic cuts (k_x vs k_y) at the H level ($E = 2.8 \text{ eV}$) and (d) at the H-1 level ($E = 3.3 \text{ eV}$) as compared to the pristine Ag(111) case.



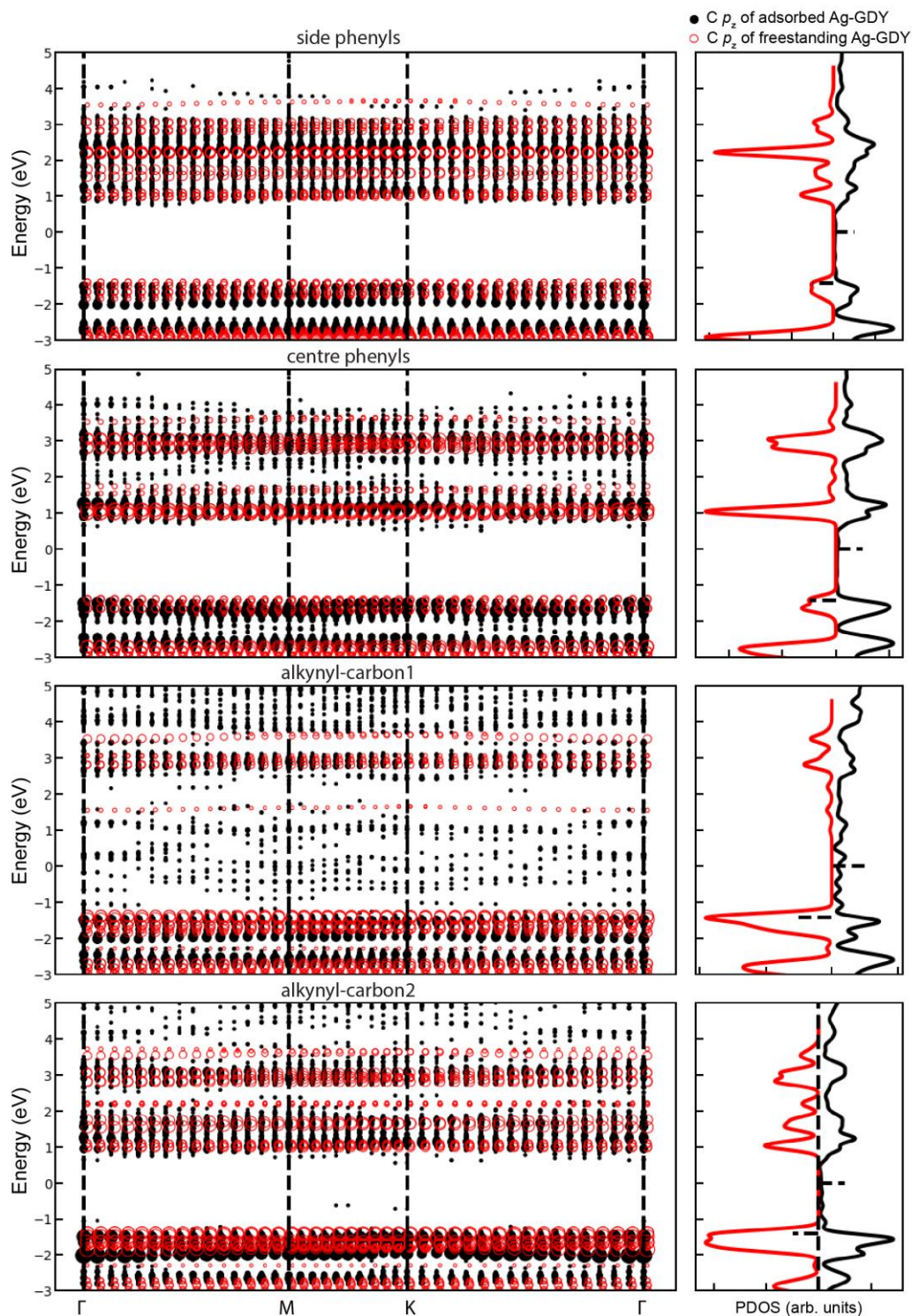
Supplementary Figure 15 | ARPES band structure in second derivative comparing Ag(111), Ext-TEB/Ag(111) and Ag-GDY network/Ag(111). ARPES band structure (E vs k_y at $k_x=0 \text{ \AA}^{-1}$) along the $[1\bar{1}0]$ direction, comparing the pristine Ag(111) (a), intact Ext-TEB multilayer (b) and Ag-GDY network (c). The localized molecular orbitals (denoted as H and H-1) in (b) evolve into valence bands (VB'_1 and VB'_2) upon the formation of the Ag-GDY network. The wide bandwidth of VB'_1 evidences the delocalized electronic states in the Ag-GDY network. No appreciable changes are observed for the substrate d -bands, which display better resolution in (c) due to the lower substrate temperature during measurement ($T_{\text{sub}} = 60 \text{ K}$) in comparison to the RT measurements in (a) and (b).



Supplementary Figure 16 | Ag-GDY ARPES band structure dependence with photon energy. (a, b) ARPES band structures (E vs k_y at $k_x=0 \text{ \AA}^{-1}$) of the Ag-GDY network along the $[1\bar{1}0]$ direction of Ag(111) measured at 62 eV (a) and 100 eV (b) photon energies, respectively. (c) Constant energy curves at different binding energies (Fermi level, 1 eV and 2 eV) extracted from the ARPES spectra in (a) and (b). Clearly the Ag sp -bands change their position with different photon energies. (d) Energy distribution curves obtained at $k_y=1.25 \text{ \AA}^{-1}$ from (a) and (b) show that the VB'_1 and VB'_2 features remain unchanged with two different photon energies, evidencing their 2D nature.



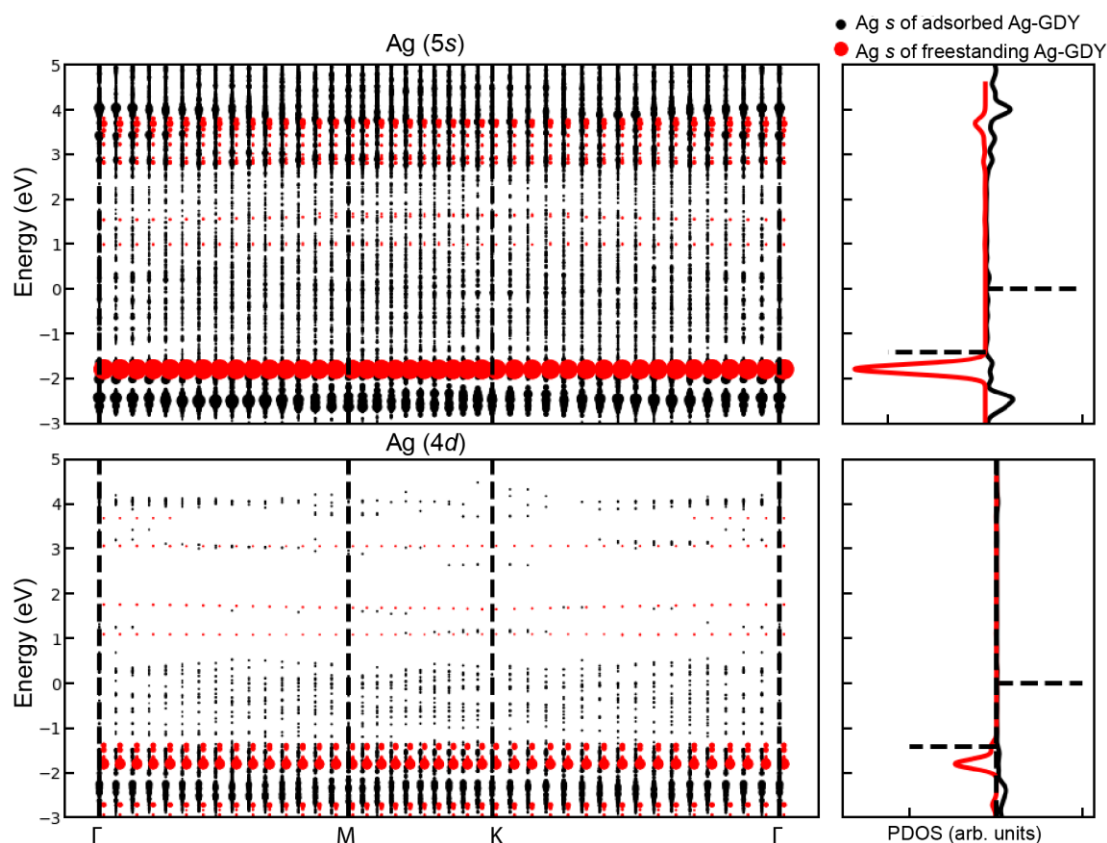
Supplementary Figure 17 | DFT-calculated nanopore-confined surface states. (a) Site-specific projected density of states of Ag-GDY network adsorbed on the four-layer Ag(111) slab. (b,c) Isosurfaces of orbital density of the whole system with two selected energies corresponding to $n=1,2$ of the nanopore-confined surface state.



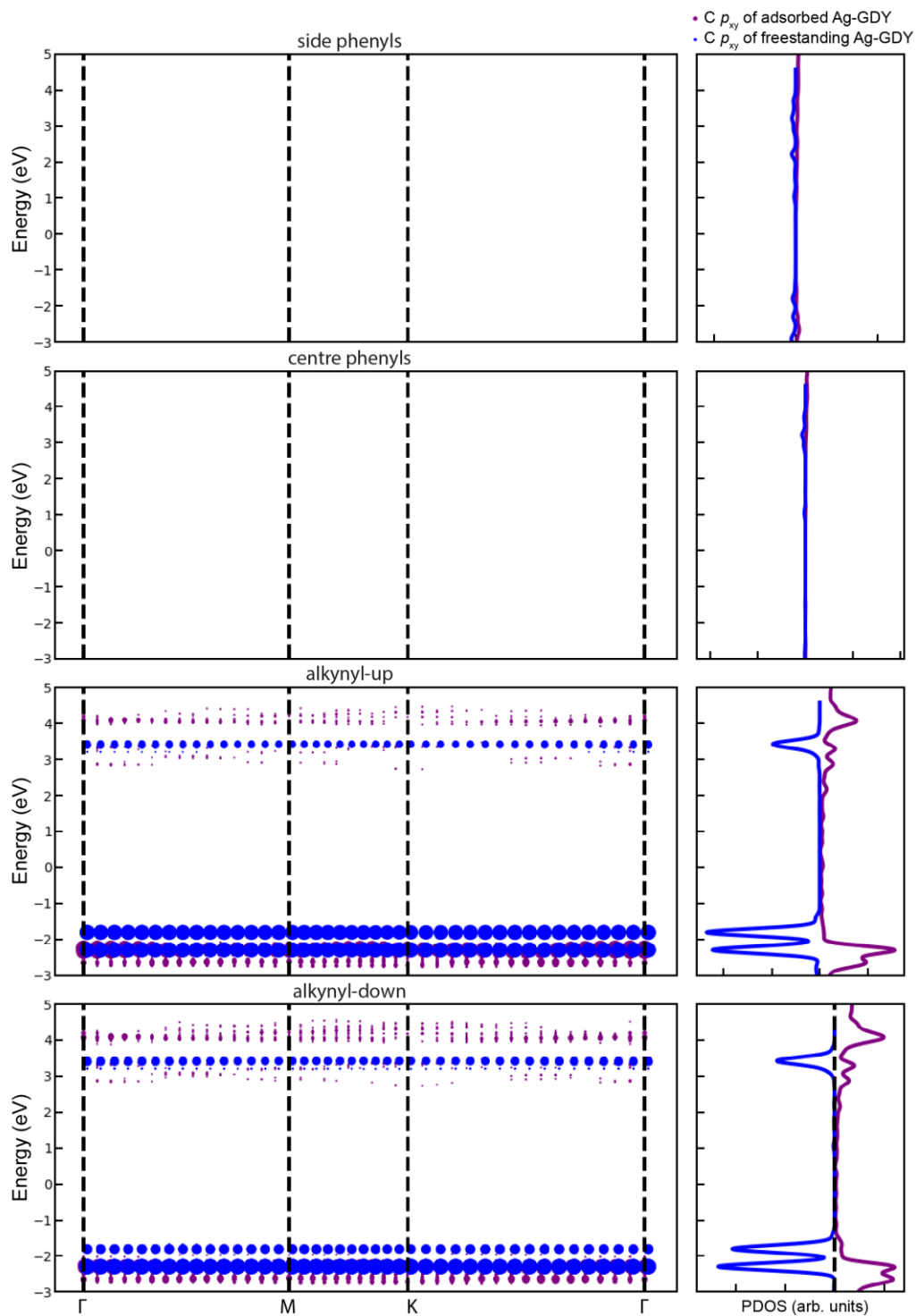
Supplementary Figure 18 | Projected band structure and DOS of carbon p_z component from phenyl rings and alkynes in the Ag-GDY network. Red circles and black dots correspond to the free-standing and the adsorbed Ag-GDY network, respectively. The Fermi levels of two systems are shifted to achieve good alignment between the band gaps. Alkynyl-carbon1/2 represents the carbon atom in the alkynyl group connecting to the phenyl-ring (or substrate).

Hybridization and charge transfer effects are well-known effects for organometallic or metal-organic nanostructures fabricated on noble metal surfaces². Note that the degree of hybridization (mild or strong) depends on the noble metal crystal used³ as well as organic system under investigation.

In our case, the band structure for the free-standing Ag-GDY sheet is moderately altered when adsorbed on the Ag(111) substrate (see Figures S18-20). This can be recognized by comparing the free-standing Ag-GDY bands (in red or blue) with the ones corresponding to the whole system (in black or purple). Due to the presence of charge transfer from the substrate to the Ag-GDY layer, PDOS peaks of freestanding and adsorbed sheets are aligned for comparison. Both peak positions as well as their widths do not show significant variation, which clearly indicates a mild hybridization degree³.



Supplementary Figure 19 | Projected band structure and DOS of Ag(5s) and Ag(4d) components from alkynyl-Ag atom in the Ag-GDY network. Red and black dots correspond to the free-standing and the adsorbed network, respectively. The Fermi levels of two systems are shifted following the value according to Supplementary Fig. 18.



Supplementary Figure 20 | Projected band structure and DOS of carbon in-plane p components from phenyl rings and alkynes in the Ag-GDY network. Blue and violet dots correspond to the free-standing and the adsorbed network, respectively. The Fermi levels of two systems are shifted following the value according to Supplementary Fig. 18.

References

1. Zhang, Y.-Q., *et al.* Synthesizing highly regular single-layer alkynyl–silver networks at the micrometer scale via gas-mediated surface reaction. *J. Am. Chem. Soc.* **141**, 5087-5091 (2019).
2. Schlickum, U., *et al.* Metal-organic honeycomb nanomeshes with tunable cavity size. *Nano Lett.* **7**, 3813-3817 (2007).
3. Harutyunyan, H., *et al.* Hybridisation at the organic-metal interface: a surface-scientific analogue of Huckel's rule? *Chem. Commun.* **49**, 5993-5995 (2013).